



## Structure of a mushy layer under hypergravity with implications for Earth's inner core

Ludovic Huguet, Thierry Alboussiere, Michael I. Bergman, Renaud Deguen, Stephane Labrosse, Germain Lesoeur

### ► To cite this version:

Ludovic Huguet, Thierry Alboussiere, Michael I. Bergman, Renaud Deguen, Stephane Labrosse, et al.. Structure of a mushy layer under hypergravity with implications for Earth's inner core. *Geophysical Journal International*, 2016, 204 (3), pp.1729-1755. 10.1093/gji/ggv554 . hal-02331124

**HAL Id: hal-02331124**

**<https://univ-lyon1.hal.science/hal-02331124>**

Submitted on 10 Sep 2021

**HAL** is a multi-disciplinary open access archive for the deposit and dissemination of scientific research documents, whether they are published or not. The documents may come from teaching and research institutions in France or abroad, or from public or private research centers.

L'archive ouverte pluridisciplinaire **HAL**, est destinée au dépôt et à la diffusion de documents scientifiques de niveau recherche, publiés ou non, émanant des établissements d'enseignement et de recherche français ou étrangers, des laboratoires publics ou privés.



Distributed under a Creative Commons Attribution 4.0 International License

# Structure of a mushy layer under hypergravity with implications for Earth's inner core

Ludovic Huguet,<sup>1,\*</sup> Thierry Alboussière,<sup>1</sup> Michael I. Bergman,<sup>2</sup> Renaud Deguen,<sup>1</sup> Stéphane Labrosse<sup>1</sup> and Germain Lesœur<sup>1</sup>

<sup>1</sup>CNRS UMR 5276, Université Lyon 1, ENS Lyon, Laboratoire de Géologie de Lyon, Terre, Planètes, Environnement, 2 rue Raphaël Dubois, Villeurbanne F-69622, France. E-mail: [ludovic.huguet@ens-lyon.org](mailto:ludovic.huguet@ens-lyon.org)

<sup>2</sup>Physics Department, Simon's Rock College, 84 Alford Road, Great Barrington, MA 01230, USA

Accepted 2015 December 28. Received 2015 November 29; in original form 2015 July 10

## SUMMARY

Crystallization experiments in the dendritic regime have been carried out in hypergravity conditions (from 1 to 1300 g) from an ammonium chloride solution (NH<sub>4</sub>Cl and H<sub>2</sub>O). A commercial centrifuge was equipped with a slip ring so that electric power (needed for a Peltier device and a heating element), temperature and ultrasonic signals could be transmitted between the experimental setup and the laboratory. Ultrasound measurements (2–6 MHz) were used to detect the position of the front of the mushy zone and to determine attenuation in the mush. Temperature measurements were used to control a Peltier element extracting heat from the bottom of the setup and to monitor the evolution of crystallization in the mush and in the liquid. A significant increase of solid fraction and attenuation in the mush is observed as gravity is increased. Kinetic undercooling is significant in our experiments and has been included in a macroscopic mush model. The other ingredients of the model are conservation of energy and chemical species, along with heat/species transfer between the mush and the liquid phase: boundary-layer exchanges at the top of the mush and bulk convection within the mush (formation of chimneys). The outputs of the model compare well with our experiments. We have then run the model in a range of parameters suitable for the Earth's inner core. This has shown the role of bulk mush convection for the inner core and the reason why a solid fraction very close to unity should be expected. We have also run melting experiments: after crystallization of a mush, the liquid has been heated from above until the mush started to melt, while the bottom cold temperature was maintained. These melting experiments were motivated by the possible local melting at the inner core boundary that has been invoked to explain the formation of the anomalously slow F-layer at the bottom of the outer core or inner core hemispherical asymmetry. Oddly, the consequences of melting are an increase in solid fraction and a decrease in attenuation. It is hence possible that surface seismic velocity and attenuation of the inner core are strongly affected by melting.

**Key words:** Core, outer core and inner core; Permeability and porosity; Composition of the core; Coda waves; Seismic attenuation; Wave scattering and diffraction.

## 1 INTRODUCTION

Due to secular cooling, the Earth's core crystallizes. As the slope of the Clapeyron profile is steeper than the adiabatic gradient, crystallization starts from the centre of the Earth. The solidification of the Earth's inner core is a major source of energy for convection in the outer core, which generates the magnetic field. Conversely, convection has an impact on the solidification processes by altering the transfer of light elements at the inner core boundary (ICB).

\* Now at: Department of Earth, Environmental, and Planetary Sciences, Case Western Reserve University, Cleveland, OH 44106, USA.

By analogy with metallurgy, Fearn *et al.* (1981) have argued that the solidification conditions at the ICB must lead to the formation of a mushy layer—a two-phase medium where solid dendrites coexist with a light-elements-rich liquid—and that ‘the mushy zone will be very thick, possibly extending to the centre of the Earth’. However, PKiKP waves show a sharp boundary at the top of the inner core from 1 s period waves (Engdahl *et al.* 1974). Moreover, observations of PKJKP waves (Okal & Cansi 1998; Deuss *et al.* 2000; Cao *et al.* 2005) denote the presence of a sharp transition at the ICB to allow the conversion of compressive waves to shear waves (Deuss 2014). These observations suggest that the transition zone at the ICB should be less than 5 km thick (Phinney 1970; Cummins & Johnson 1988a;

Kawakatsu 2006; Deuss 2014) and this sharpness seems to be at odds with the presence of a thick mushy layer. The conditions at the ICB are strongly affected by the vigorous convection in the outer core (Fearn *et al.* 1981; Loper & Fearn 1983; Shimizu *et al.* 2005; Deguen *et al.* 2007; Alexandrov & Malygin 2011). In this paper, we aim at reconciling seismological observations with the existence of a mushy zone by studying the importance of vigorous convection on crystallization of an alloy.

The shear velocity contrast at the ICB is estimated using normal modes (Dziewonski & Anderson 1981), body waves (PKP and PKiKP) (Häge 1983; Choy & Cormier 1983; Cummins & Johnson 1988b), and PKiKP/PcP amplitude ratios (Engdahl *et al.* 1970; Souriau & Souriau 1989; Shearer & Masters 1990; Cao & Romanowicz 2004; Zeng & Ni 2013). From all methods, the shear velocity jump ranges between 0 to 4 km s<sup>-1</sup>. However, Shearer & Masters (1990) estimated the lower limit at 2.5 km s<sup>-1</sup>, which is in agreement with the later studies suggesting 2–3 km s<sup>-1</sup> (Cao & Romanowicz 2004), 2.82 km s<sup>-1</sup> (Koper & Dombrovskaya 2005) and 3.2 to 4 km s<sup>-1</sup> (Zeng & Ni 2013). The analysis of PKJKP (Deuss *et al.* 2000; Cao *et al.* 2005) and normal modes (Dziewonski & Anderson 1981) give consistent values of the shear velocity in the inner core ( $\approx 3.6$  km s<sup>-1</sup>).

In a two-phase medium, the shear velocity is a decreasing function of the amount of melt (Hashin & Shtrikman 1963), so that the shear velocity could be used to constrain the solid fraction below the ICB (Loper & Fearn 1983) or in the bulk of the inner core (Vočadlo 2007). By assuming that the shear velocity given by normal modes corresponds to the zero melt fraction limit (Loper & Fearn 1983) and taking  $V_s = 2.75$  km s<sup>-1</sup> for the shear wave velocity just below the ICB, the model of Hashin & Shtrikman (1963) gives a solid fraction  $60 \pm 7$  per cent just below the ICB. However, Martorell *et al.* (2013, 2015) found that the shear velocity decreases significantly close to the melting point, which implies that the low value of the shear velocity at the ICB could be due to the proximity to the melting point rather than to the presence of melt. The density jump observed by the normal modes and the body waves is also poorly constrained (between 0.52 kg m<sup>-3</sup> and 1.66 kg m<sup>-3</sup> (Souriau & Souriau 1989; Masters & Gubbins 2003; Koper & Pyle 2004; Koper & Dombrovskaya 2005; Tkalčić *et al.* 2009)). This jump is not only due to the phase change between solid and liquid but also to the differences of concentration in light elements between outer core and inner core, or to the presence of liquid just below the ICB.

Seismological studies show a complex image of the inner core. PKiKP waves reveal a depth dependence of velocity and attenuation of *P*-waves and exhibit east–west hemispherical differences in the isotropic wave speed, elastic anisotropy, attenuation, and attenuation anisotropy in the Earth's inner core (Tanaka & Hamaguchi 1997; Irving & Deuss 2011; Waszek & Deuss 2011; Deguen 2012; Lythgoe *et al.* 2013; Deuss 2014; Tkalčić 2015). These hemispherical differences may be due to an east–west translation with enhanced solidification on one side and melting on the other (Alboussière *et al.* 2010; Monnereau *et al.* 2010). Inner core translation may lead to the formation of a dense layer at the base of the outer core due to the release of Fe-rich liquid (Alboussière *et al.* 2010). This so-called ‘F-layer’, possibly generated by inner core translation, is inferred from the observations of PKP waves as a low-velocity zone (Souriau & Poupinet 1991; Song & Helmberger 1995; Yu *et al.* 2005). Long-term mantle control over outer core convection (Sumita & Olson 1999; Aubert *et al.* 2008; Gubbins *et al.* 2011) might also explain the hemispherical differences through variations of the flow in the outer core due to the variations of heat flux at the core–mantle boundary. The heat flux may locally reverse towards the inner core

causing melting (Gubbins *et al.* 2011). It is however unclear how a nearly perfect hemispherical dichotomy could be created from this scenario. Observations of PKiKP coda due to scattering also show that there are small-scale ( $\sim 1$  km) heterogeneities at the ICB or in the uppermost inner core (Vidale & Earle 2000; Koper *et al.* 2004; Koper & Dombrovskaya 2005; Cormier 2007; Leyton & Koper 2007; Attanayake *et al.* 2014). However, the heterogeneities at the ICB do not show clear differences between west and east hemispheres (Cormier 2007; Leyton & Koper 2007).

At the ICB, the existence of a mushy layer is suggested by several theoretical studies (Fearn *et al.* 1981; Loper & Fearn 1983; Shimizu *et al.* 2005; Deguen *et al.* 2007; Alexandrov & Malygin 2011). Few directional solidification experiments applied to the inner core have been performed (e.g. Tait & Jaupart 1992; Bergman *et al.* 2005). Fearn *et al.* (1981) suggested that the mushy layer could extend to the Earth's core centre. However, its solid fraction is expected to increase rapidly due to the large convective heat and solute fluxes above the mushy layer (Worster 1991), that is consistent with a sharp transition at the ICB (Loper 1983). Bergman & Fearn (1994) have predicted that convection in the mushy layer could be very vigorous. For the mushy layer in the inner core, the compaction cannot be ignored. Sumita *et al.* (1996) proposed a model of compaction of a passive viscous medium which they applied to the inner core. They have estimated the thickness of mushy layer between 1 and 10 km depending on the viscosity of the inner core.

During the solidification of binary alloys, a mushy layer is formed from the morphological instability of the solidification front, the so-called ‘Mullins–Sekerka instability’ (Mullins & Sekerka 1964; Davis 2001). This instability is caused by undercooling associated with the release of light elements above the solid/liquid interface. The decrease of liquidus temperature ahead of the crystallization front can be such that it falls below the actual temperature profile. Morphological instabilities of the solid/liquid interface develop, forming small needles or dendrites. The mush itself can be subjected to two buoyancy-driven convective instability modes (Worster 1992): the boundary-layer mode and the mushy-layer mode. The first one is due to the instability of the compositional boundary layer ahead of the mush and is associated with salt finger convection in the liquid region ((1) in Fig. 1). The boundary-layer mode is the first mode to be active while the interstitial liquid remains stagnant (Tait & Jaupart 1989; Chen & Chen 1991; Chen 1995). When the thickness of the mushy layer reaches a critical value, the mushy-layer mode becomes the main mode and leads to the formation of chimneys ((2) in Fig. 1) due to the dissolution of dendrites (Tait & Jaupart 1992) in regions of upwelling which extend in the liquid in the form of laminar or meandering plume ((3) in Fig. 1). These two modes extract the solute rejected during solidification.

Jackson *et al.* (1966) suggested using an ammonium chloride solution as an analogue to metallic alloys. McDonald & Hunt (1970) and Copley *et al.* (1970) studied experimentally the solidification process using this solution, and they observed the formation of chimneys in the mushy layer. Chimneys are also observed in metallic alloys (e.g. Sarazin & Hellawell 1988; Bergman *et al.* 1997). The fluid motions in the mushy layer are well documented by experimental (e.g. Chen & Chen 1991; Tait & Jaupart 1992; Worster & Wettlaufer 1997) and numerical studies (e.g. Worster 1997; Rees Jones & Worster 2013; Wells *et al.* 2013).

Most studies have been restricted to a regime where convective flow speed is comparable to the velocity of the solidification front whereas this ratio is around  $10^7$  in the core. One implication is that convective solute and heat transport is expected to have a comparatively larger impact on the resulting mushy layer structure and

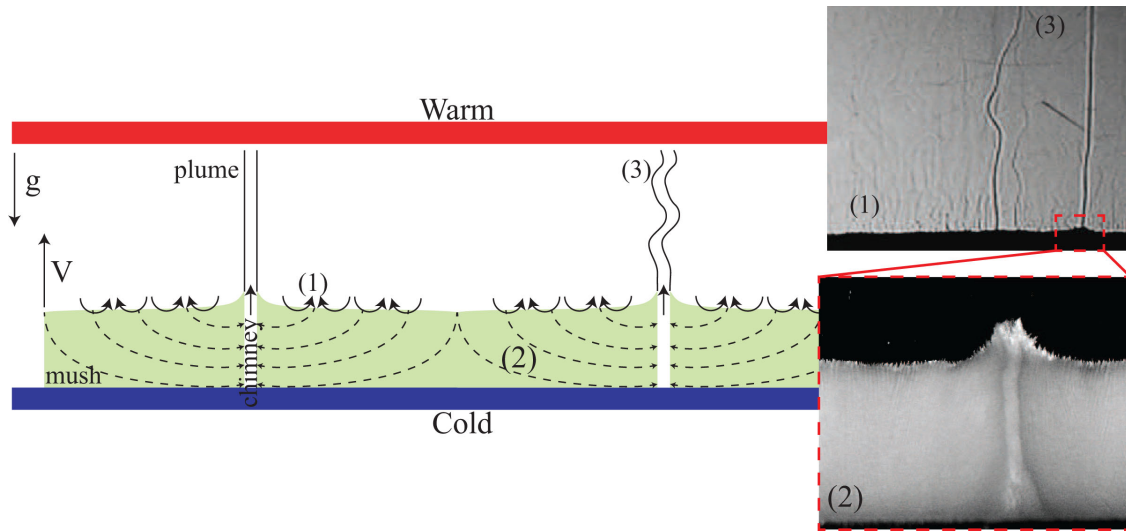


**Figure 1.** Schematic view of directional solidification cooled from below in a Hele-Shaw cell and pictures from an actual experiment using an ammonium chloride solution. The solidification leads to fluid motions in a mushy layer and in the liquid above. The boundary-layer mode of convection is only associated with salt fingers when there is also a stable thermal buoyancy gradient (1). A mushy-layer mode leads to the formation of chimneys in the mush (2) and laminar or meandering plume (3).

dynamics at the ICB. Worster (1991) has shown that an increase of this ratio leads to a decrease of the height of mushy layer and increase of its solid fraction. To reach conditions under which the ratio of the convective velocity to solidification rate is large, we study the solidification of an ammonium chloride solution under hypergravity (up to 1300 g) using a centrifuge in order to increase the vigour of convection. Some previous studies have already used a centrifuge in metallurgy (e.g. Müller & Neumann 1983; Rodot *et al.* 1986, 1990; Battaile *et al.* 1994) to increase the apparent gravity (up to about 15 g) and observed an effect of increasing  $g$  on the microstructure of the mushy layer, essentially a reduction in the primary interdendritic spacing.

Motivated by the inner core translation model (Alboussière *et al.* 2010; Monnereau *et al.* 2010) which causes melting on one hemisphere, we are also interested in a mushy layer melted from above. We have thus performed crystallization experiments after which we have been heating the top of the mushy layer from above while maintaining a cold temperature at the bottom. Some experimental studies have already been carried out on melting a mushy layer (Hallworth *et al.* 2004, 2005; Yu *et al.* 2015). Hallworth *et al.* (2004) observed an unexpected result: the melting of a reactive porous medium leads to recrystallization of the sinking interstitial liquid and produces a layered structure in the bulk. In Pb–Sn directional solidification experiment, heating and melting the mushy layer from above lead to the sinking and recrystallization of the melted Pb liquid (Yu *et al.* 2015). The heavy melt produced by melting drives compositional convection which redistributes this melt in the lower layer. The crystallization of this melt leads to an increase of the solid fraction (Hallworth *et al.* 2004, 2005; Butler *et al.* 2006; Butler 2011).

In both solidification and melting experiments, we have used ultrasonic waves as analogues to the seismic waves to probe the microstructure of the mushy layer. We have measured the scattering and the attenuation which depend on the solid fraction and interdendritic spacing. These measurements can help not only to characterize the experiments but also to interpret the core phases in the seismic waves and unravel the mushy layer structure at the ICB.

The paper is outlined as follows. In Section 2, we introduce the experimental protocol used during the solidification and melting experiments. All experimental results are presented in Section 3.

We have measured the evolution of the thickness of the mushy layer at different gravity values, and probed the microstructure of the mush with ultrasounds to measure their attenuation in a mushy layer during a melting or solidification experiments. In Section 4, we introduce a mathematical model describing the macroscopic evolution of a mushy zone with kinetic under-cooling and we compare our experimental results with the model. Based on a simplified model, we analyse the dimensionless parameters dependence of the evolution of the mushy layer in the Section 5. The good agreement between the two allows us to apply our model to the crystallization of the inner core and obtain conditions under which large solid fraction can be obtained below the ICB (see Section 6). We discuss our main results in Section 7.

## 2 EXPERIMENTAL PROTOCOL

We use a Beckman J-26 XPI centrifuge to increase the apparent gravity up to 1300 g (Fig. 2). The rotor consists of four buckets, two of which being empty. The other buckets contain the experimental cell ((1) in Fig. 2) and a counterweight ((3) in Fig. 2). Each bucket is free to tilt itself according to the local gravity field (sum of Earth gravitation and centrifugal forces), depending on the rotation rate (i.e. for a large rotation rate, each bucket is nearly perpendicular to the rotation axis). A slip ring allows us to connect the on-board electronics to the acquisition board ((2) in Fig. 2) and provides electric power to the experiment. The details of the experimental protocol can be found in Appendix A.

Fig. 3 presents a longitudinal cross-section of the cell crossing the ultrasonic probes. The ‘bottom’ and the ‘top’ of the cell are defined according to the local gravity vector (green arrow) which controls the tilt of the buckets as function of rotation rate. The lateral boundary of the cell consists of four Perspex walls ((5) in Fig. 2), 1 cm thick, surrounded by a perspex tube of thickness 1.5 cm ((6) in Fig. 2) and by the bucket ((7) in Fig. 2). At the bottom, a Peltier element is used to cool the cell from below ((4) in Fig. 2). It is able to extract around 20 W. At the top, there is a (resistive) heater element able to provide around 6 W. Five temperature probes PT100 are placed on one wall at 3, 16, 28, 40 and 61 mm from the

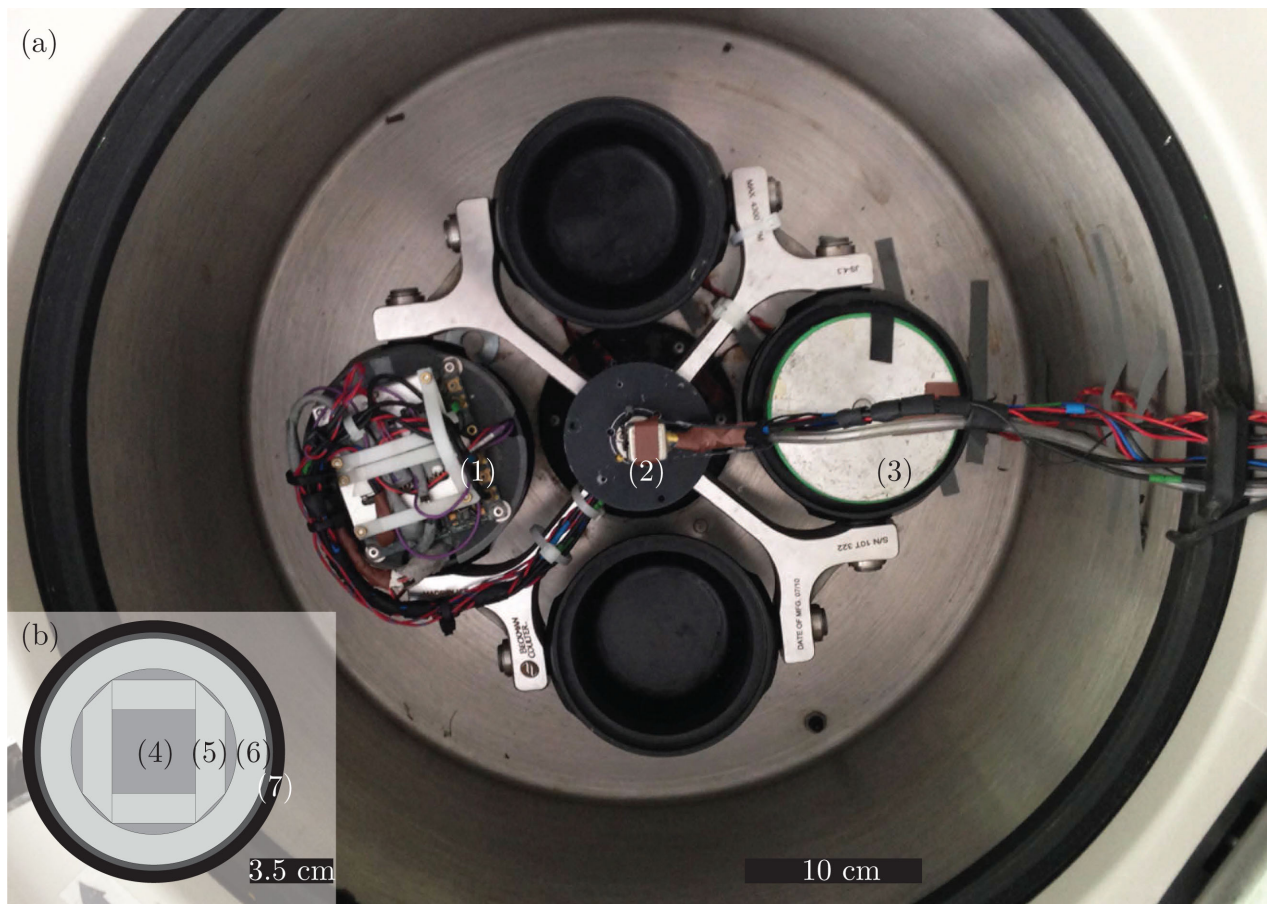


**Figure 2.** (a) Beckman J-26 XPI centrifuge with the rotor composed of four buckets. Two buckets contain the experimental cell (1) and the counterweight (3). A slip ring (2) with 10 channels allows connecting the cell to the acquisition and control cards. (b) Schematic top view of the experimental cell in the bucket (1). (4) is the Peltier element at the bottom of the cell. (5) and (6) are the thermal insulation of the cell, which are surrounded by the bucket (7).

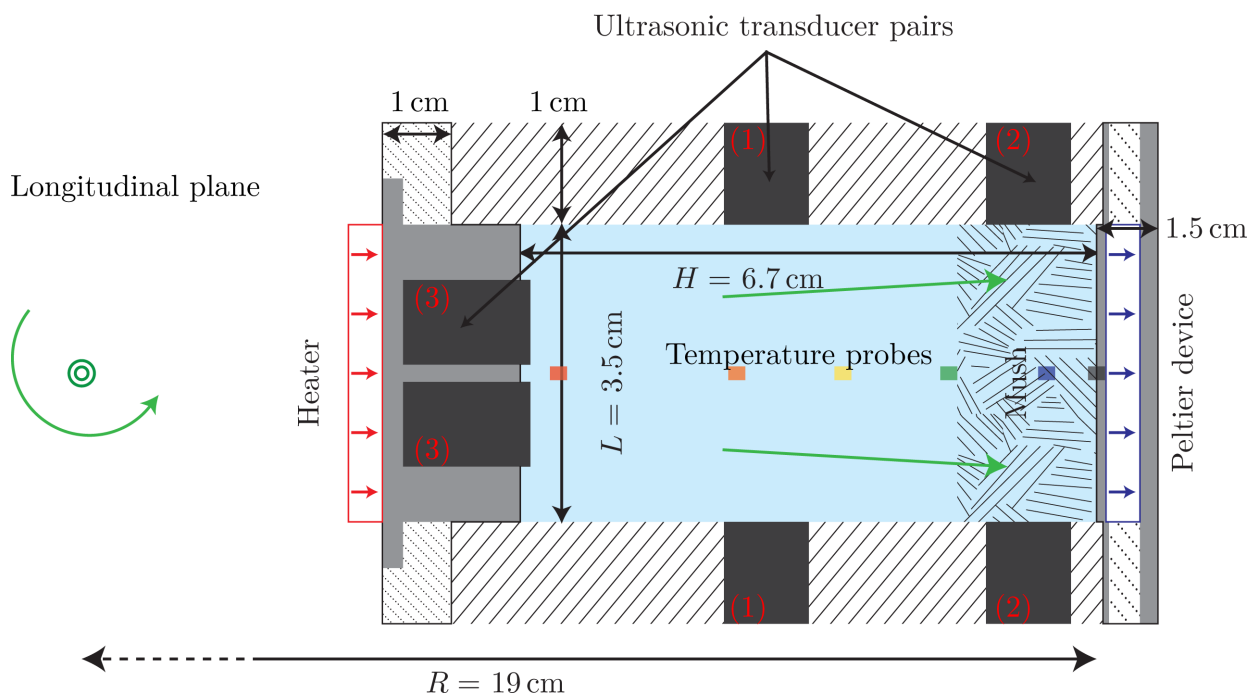


**Figure 3.** Longitudinal plane of the cell crossing the ultrasonic probes. The gravity is towards the right (green arrows). The dimensions of the cell are  $6.7 \times 3.5 \times 3.5 \text{ cm}^3$ . The bottom of the cell is 19 cm away from the axis of rotation.

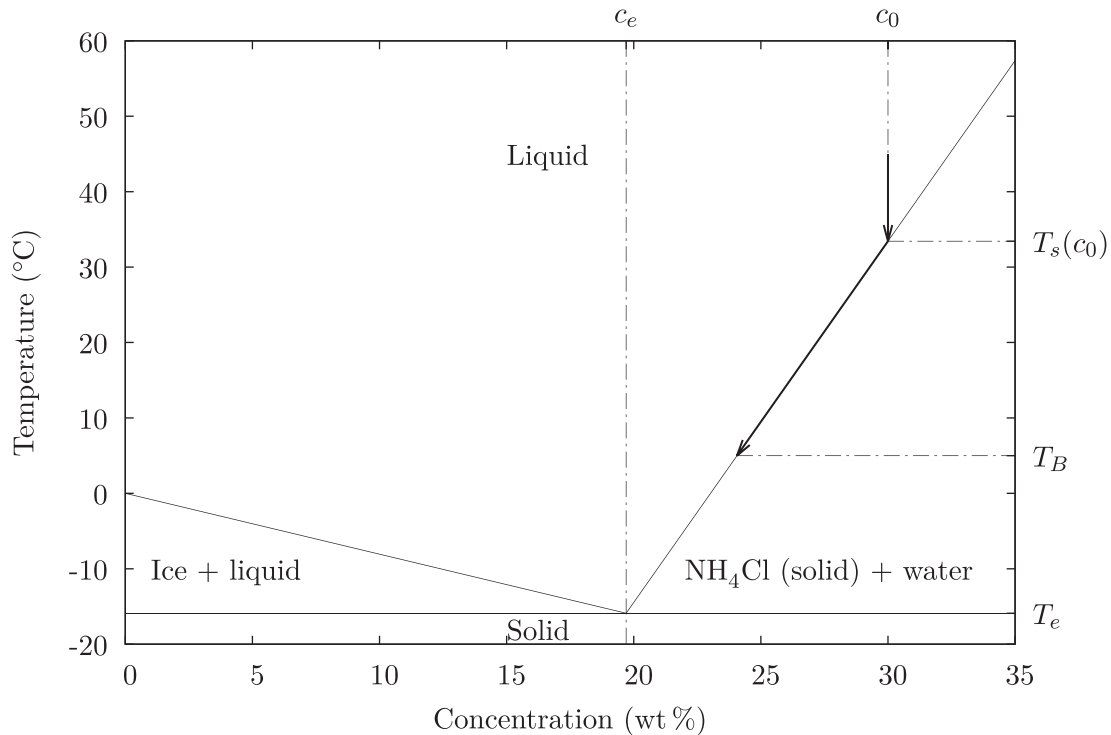


**Figure 4.** Phase diagram of aqueous ammonium chloride solution. On the water-rich side of the eutectic point (with freezing temperature  $T_e$ ), the solidified solid is ice, while on the  $\text{NH}_4\text{Cl}$ -rich side of the eutectic point, right-hand-side on this figure, solid formed is almost purely ammonium chloride  $\text{NH}_4\text{Cl}$ . The black arrow denotes the theoretical path of temperature and concentration liquid from an initial solution at 30 wt per cent and  $45^\circ\text{C}$  cooled from the bottom at a target temperature  $T_B$ .

bottom. Another temperature probe is placed on the Peltier device. Furthermore, we use three pairs of ultrasonic transducers to send a sweep between 1.8 and 6 MHz to measure the thickness of the mush during the experiments under rotation, and to probe its structure. The first transverse pair of transducers is used to measure the sound velocity in the liquid ((1) in Fig. 3). The second one allows us to determine the velocity and the attenuation in the mushy layer ((2) in Fig. 3). Finally, a vertical pair of transducers gives access to the height of the mush and the attenuation ((3) in Fig. 3).

At the bottom of the cell, the temperature is maintained at around  $5^\circ\text{C}$  by the Peltier element with a PID controller, that is, a control loop feedback mechanism to cancel the temperature fluctuations in the centrifuge due to a poor temperature control (Fig. 5). We use an aqueous solution of ammonium chloride  $\text{NH}_4\text{Cl}$ . The initial concentration is 30 wt per cent and the initial temperature is around  $45^\circ\text{C}$  (Fig. 4). We have carried out solidification experiments at 1, 13, 208 19, 26, 76, 119, 136, 478 and 1327 g and melting experiments at 1, 13, 136 and 478 g. The gravity value is defined at the bottom of the cell and is 35 per cent smaller at the top of the cell. We have also run experiments in a transparent tank ( $15 \times 15 \times 7.5 \text{ cm}^3$ ) at 1 g, that is, in the non-rotating frame, to observe visually the growth of the mush, convection in the liquid and the effects of the melting from above. In these experiments, we took pictures every minute.

### 3 EXPERIMENTAL RESULTS

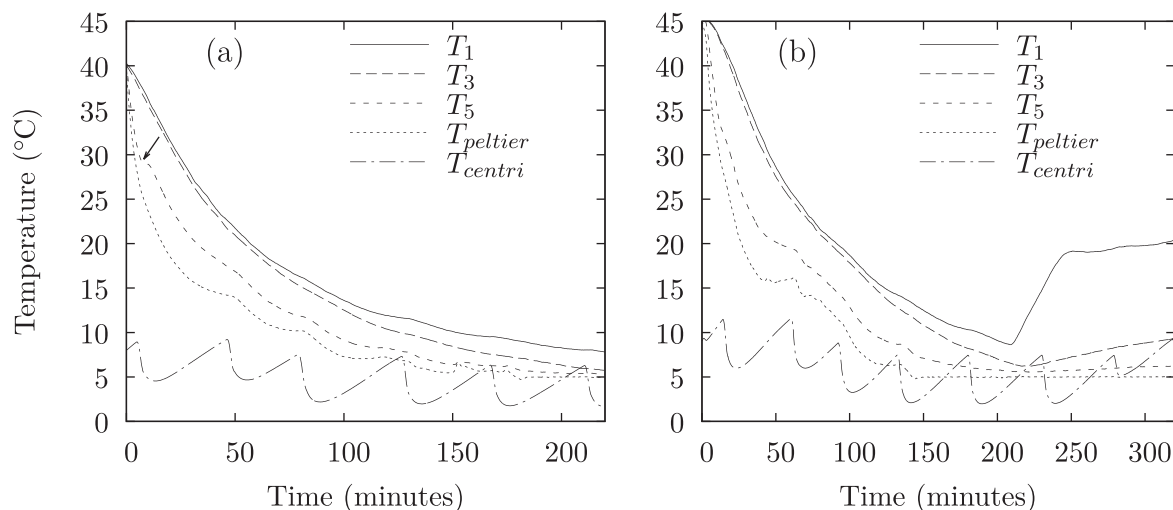
#### 3.1 Thermal evolution in the liquid

Fig. 5 shows the typical evolution of temperatures during two different solidification experiments at 13 g. One of these experiments

(Fig. 5b) is followed by a phase of heating from above (from  $t \simeq 210$  min) causing partial melting of the mush. From its initial temperature, the liquid is cooled from below with a temperature prescribed to  $5^\circ\text{C}$  at its bottom during 240 min for the solidification experiments and 330 min for the melting experiments. It takes typically 100 min after the beginning of crystallization to actually reach the target temperature (Fig. 5). The initial temperature can be different between different runs, but this does not matter as long as it is above the initial melting point of the liquid: it will only change the starting time of crystallization. The oscillations of the temperature measured in the centrifuge,  $T_{\text{centri}}$ , nearly periodic over a typical time of 40 min and amplitude about  $5^\circ\text{C}$ , are due to the poor control of the machine. The change of slope of the temperature curve corresponding to the probe just above the Peltier element (dashed line, marked by a small arrow) is due to the onset of crystallization. At this time (7 min), the interface temperature is around  $28^\circ\text{C}$ , that is,  $7^\circ\text{C}$  lower than the equilibrium solidification temperature  $T_s(c_0) = 34.57^\circ\text{C}$ . The crystallization produces a release of latent heat that explains this change in slope. During a melting experiment, the heater is turned on when the temperature in the liquid is smaller than  $10^\circ\text{C}$ , while the bottom temperature is maintained at  $5^\circ\text{C}$ . At the top, the temperature increases to  $20^\circ\text{C}$ .

#### 3.2 Evolution of the mushy layer height and solid fraction

The ultrasonic signal sent by the transducers is a 7.5 ms long linear sweep with frequencies ranging from 1.8 to 6 MHz. The recorded signals are cross-correlated with the theoretical sweep sent by the transducers. This produces a signal equivalent to that from an impulsive source. Fig. 6 shows the evolution of the cross-correlated signals sent and recorded by the vertical pair of ultrasonic probes ((3) in Fig. 3) during a solidification experiment at 478 g. We have



**Figure 5.** Evolution of the temperatures in the liquid during two different solidification experiments at 13 g. In panel (b) crystallization is followed by a melting experiment.  $T_{\text{centri}}$  and  $T_{\text{peltier}}$  denote the temperature in the centrifuge and at the surface of the Peltier device respectively. The 5 °C oscillations of  $T_{\text{centri}}$  are due to the ‘On/Off’ loop temperature control of the centrifuge.  $T_{1,3,5}$  are temperatures at three different heights (3, 28 and 61 mm). The arrow at time 7 min points to a kink in the curve of  $T_5$  associated with the onset of crystallization.

picked the arrival time, that is, the first reflection at the surface of the mushy layer (black dots in Fig. 6) to determine the thickness of the mushy layer (see Fig. 7). However, this arrival is not always clear because the mushy layer is a scattering medium at this frequency range. The first arrival is followed by a coda which demonstrates the presence of scattering in the mush (Aki & Chouet 1975).

From the signal recorded with the vertical pair of ultrasonic transducers (Fig. 6), we track the evolution of the thickness of the mushy layer (Fig. 7a). The evolution of the mushy layer height starts as independent of gravity but levels off to a final value that decreases with gravity. Tait & Jaupart (1992) have carried out experiments of directional solidification of aqueous ammonium chloride solutions, in relatively similar conditions, in which they used a small amount of polymerizing agent to increase the viscosity. They have shown that the final height increases with the liquid viscosity (Fig. 7b). The decrease of the final height with increasing  $g$  observed in our experiments (Fig. 7a) is consistent with the experimental results of (Tait & Jaupart 1992; Fig. 7b) if the final height is assumed to be a function of mushy layer Rayleigh number of the liquid,  $R_m$ , only (the other control parameters being equal in both studies). Since  $R_m \propto g/\eta$ , increasing  $\eta$  is equivalent to decreasing  $g$ . We can therefore transpose the viscosity values in Tait & Jaupart’s (1992) experiments to equivalent gravity values. For example, an experiment performed at 1 g with a 16 mPa s viscosity melt corresponds to an experiment at 0.09 g with the 1.5 mPa s viscosity of our experiments. The evolution of the mush thickness diverges earlier and earlier from the conductive solution (dashed line in Fig. 7b) when gravity is increased or viscosity is decreased. This behaviour is consistent with an increase of the vigour of convection in the mushy layer compared to its solidification rate (Worster 1991).

The main result of the experiments under hypergravity is the decrease in the final height of the mush with gravity. Fig. 8 shows the final thickness and solid fraction (red square) as functions of gravity. We measure the thickness of the mush postmortem (black circle) and from the ultrasonic signals (blue circles). The discrepancy between the two is due to: (i) the difficulty to pick the first-arrival in the ultrasonic signals (Fig. 6), because the mushy layer is a scattering medium and (ii) the uncertainty on the sound velocity. We use the transverse transducer pairs ((1) in Fig. 3) to determine the sound

velocity in the liquid which is assumed uniform (corresponding to a uniform temperature). We estimate the error on the determination of height to be  $\sim 1.5$  mm.

We can write the solid fraction  $\Phi$  as

$$\Phi = \frac{M_{\text{solid}}}{\rho_s V_{\text{mush}}} \quad (1)$$

where  $\rho_s$  is the density of solid  $\text{NH}_4\text{Cl}$ ,  $M_{\text{solid}}$  is the mass of solid  $\text{NH}_4\text{Cl}$  at the end and  $V_{\text{mush}}$  is the volume of the mushy layer, that is,  $V_{\text{mush}} = h \times 3.5 \times 3.5 \text{ cm}^3$ . We estimate  $M_{\text{solid}}$  assuming thermodynamic equilibrium. Because approximately the same quantity of  $\text{NH}_4\text{Cl}$  crystallizes in the different experiments, the decrease of height corresponds to an increase of solid fraction with gravity (Fig. 8).

### 3.3 Interdendritic spacing measurements

We measure the primary interdendritic spacing  $\lambda_1$  from pictures taken under a binocular microscope with a magnification between 20 and 100 $\times$ . However, the measurement is difficult and we have obtained only three value at three different gravity values 13, 136 and 305 g. Fig. 9 shows that  $\lambda_1$  decreases with gravity. Several studies have shown that vigorous convection in the interstitial liquid generated by higher apparent gravity or by magnetic fields leads to a decrease in interdendritic spacing (Battaille *et al.* 1994; Lehmann *et al.* 1998; Chen *et al.* 2003; Tewari & Tiwari 2003; Spinelli *et al.* 2005, 2006; Diepers & Steinbach 2006; Steinbach 2009; Viardin *et al.* 2014). We compare our results to three analytical models of Lehmann *et al.* (1998), Diepers & Steinbach (2006) and Steinbach (2009). Note that these studies use a Bridgman furnace, which controls the velocity of crystallization and temperature gradient independently, while neither is controlled in our experiment. The aforementioned studies proposed that  $\lambda_1 \propto g^\alpha$  with an exponent  $\alpha$  between  $-1/4$  and  $-1/8$ . Our results are more consistent with  $\lambda_1 \propto g^{-1/4}$ , although the uncertainty of the control parameters and the scarceness of our data do not allow us to conclude. The analysis in Lehmann *et al.* (1998) is adapted from (Kurz & Fisher 1981) as interdendritic velocity is substituted to the growth rate in the determination of the typical undercooling near the tips of dendrites. We

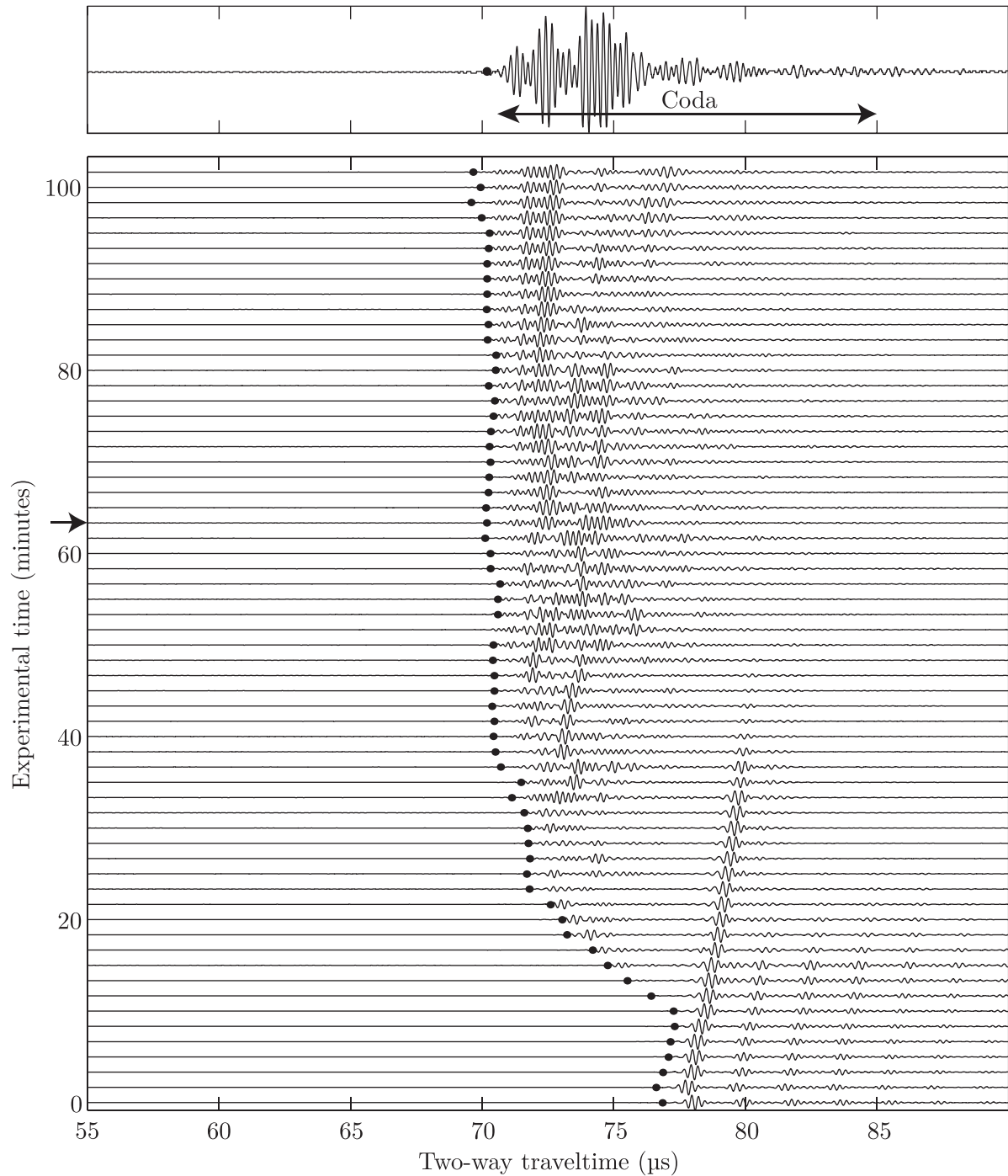


**Figure 6.** Evolution of ultrasonic signal from the vertical pairs of transducers ((3) in Fig. 3) during a solidification experiment at 478 g. Top, a zoom on ultrasonic signal at 63.3 min as indicated by arrow on the left in the bottom panel. The black dot denotes the position of the first arrival. Each line is normalized by its maximum.

furthermore assume here that the interdendritic convective velocity scales linearly with the gravity level: this leads to  $\lambda_1 \propto g^{-1/4}$ .

### 3.4 Melting experiments

Motivated by several studies which suggest melting on one hemisphere of the inner core (Alboussière *et al.* 2010; Gubbins *et al.* 2011), we have carried out directional solidification experiments, producing mushy layers which are subsequently heated from above.

These experiments have been realized in a tank and in a centrifuge. Due to the heating from above, the mushy layer melts and the thickness decreases slowly (Fig. 10).

Fig. 11 shows the evolution of liquid convection above the solidification front using a transparent tank outside the centrifuge at 1 g. During the crystallization of the mushy layer, convection in the mush produces plumes in the liquid and chimneys in the mushy layer (Fig. 11,  $t = 0$  min). The plumes are laminar and meandering. The cones at the solid/liquid interface are due to the difference

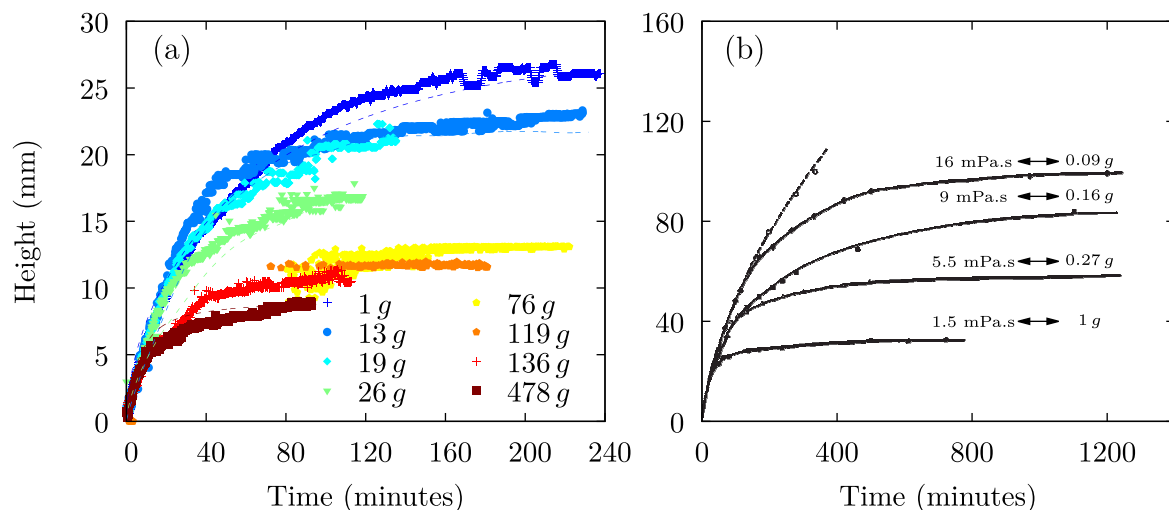


**Figure 7.** (a) Height of the mushy layer as a function of time for different apparent gravities. Squares are the experimental results and dashed lines are predictions from the evolution model presented in Section 4. (b) Fig. 7 of Tait & Jaupart (1992) for different viscosities which correspond to different gravity levels given purely as an indication. (For interpretation of the references to colour in this figure legend, the reader is referred to the web version of this paper.)

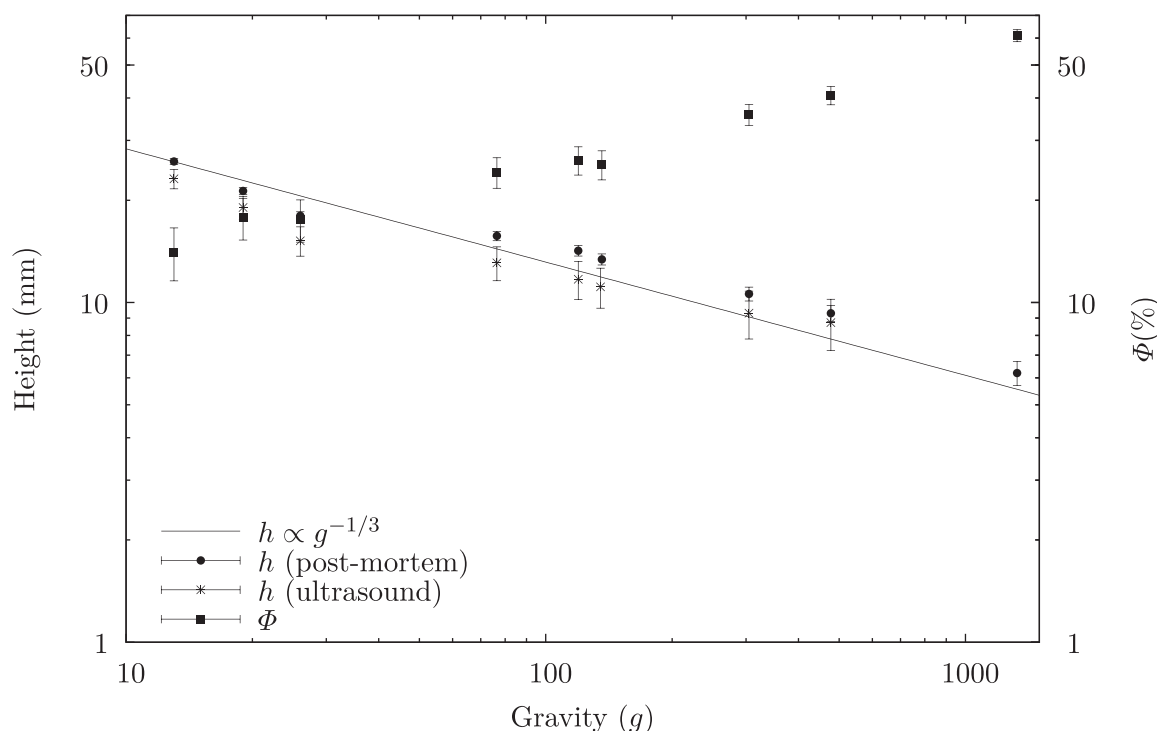


**Figure 8.** Height of mushy layer (circles and stars) and solid fraction (square) as a function of gravity. The thickness of the mush is measured postmortem (circles) and from the ultrasonic signals (stars).

between the thermal and solute diffusivity. The liquid in the vicinity of plumes is cooled by the cold and depleted liquid expelled by the chimneys whereas its composition is left unchanged because of the much smaller solute diffusivity. The melt becomes saturated and crystallizes in the form of cones. In the liquid, the temperature gradient is stabilizing, that is, the liquid is thermally stably stratified, while the gradient of solute is destabilizing due to the release of a  $\text{NH}_4\text{Cl}$ -depleted liquid during the solidification. Moreover, horizontal layers appear in the liquid and are produced by double-diffusive convection (Turner 1979), which can exist when the concentration and temperature gradients have opposite signs and when the ratio of diffusivity is large (Huppert & Turner 1981; Beckermann &

Viskanta 1988; Chen 1997). The  $\text{NH}_4\text{Cl}$ -depleted liquid carried by the plumes accumulates at the top of the box from which a stable compositional stratification develops and propagates downward, the ‘filling box mechanism’ of Baines & Turner (1969). After 260 min of solidification, we impose a constant temperature of  $60^\circ\text{C}$  at the top of the box to heat and melt the mushy layer. In the liquid part, the plumes become turbulent, with the conical shape typical of turbulent plumes (Morton *et al.* 1956; Turner 1979), indicating that convection is probably more vigorous when the mush is heated from the top (Fig. 11,  $t = 268, 294$  and  $320$  min). We interpret this to be due to an increase of the interface temperature and of the temperature difference across the mush, which corresponds to an increase of

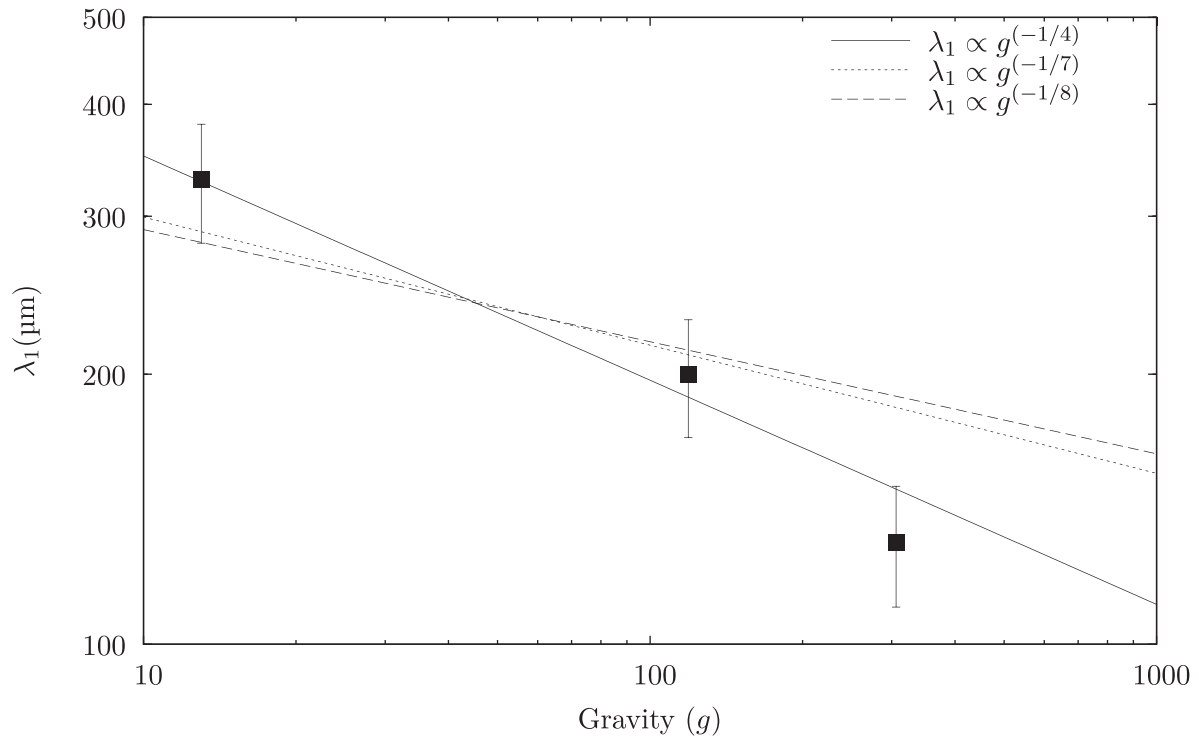


**Figure 9.** Primary interdendritic spacing  $\lambda_1$  as function of gravity  $g$ . Squares are our measurements at 13, 136 and 305  $g$ . Solid, dotted and dashed lines correspond to three theoretical models:  $\lambda_1 \propto g^{-1/4}$  adapted from (Lehmann *et al.* 1998),  $\lambda_1 \propto g^{-1/7}$  (Steinbach 2009) and  $\lambda_1 \propto g^{-1/8}$  (Diepers & Steinbach 2006), respectively.

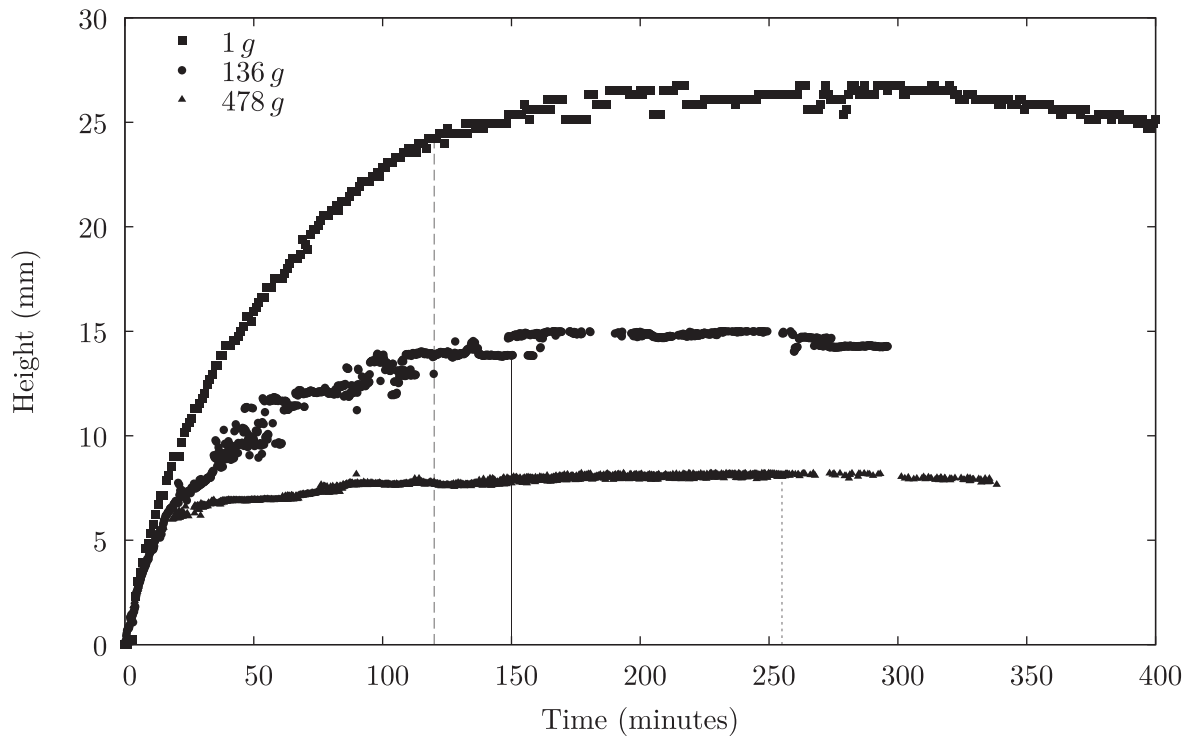


**Figure 10.** Evolution of the mush height during crystallization/melting experiments. Vertical dashed, solid and dotted lines denote the beginning of heating from above for the experiments at 1, 136 and 478  $g$ , respectively.

the concentration difference (see phase diagram on Fig. 4) since the mush must be close to thermodynamic equilibrium. After 320 min, the plumes are still active but the chimney cones disappear. The turbulent regime of the plumes prevents the formation of cones be-

cause the small scale transport of the temperature and concentration fields are now similar, in contrast to the case of laminar plumes. The melting of the mushy layer produces a  $\text{NH}_4\text{Cl}$ -rich liquid layer at the interface (Fig. 11,  $t = 320$  min).

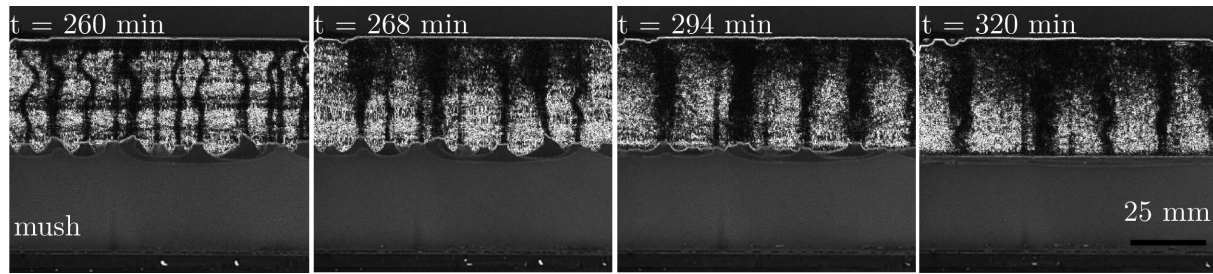


**Figure 11.** Evolution of convection in the liquid and in the mushy layer during the melting experiment at 1g. The images are composite images. In the liquid part, we have used a Schlieren technique with a random background pattern and a smoothing technique. The image of the mushy layer is a straightforward image from a digital camera.

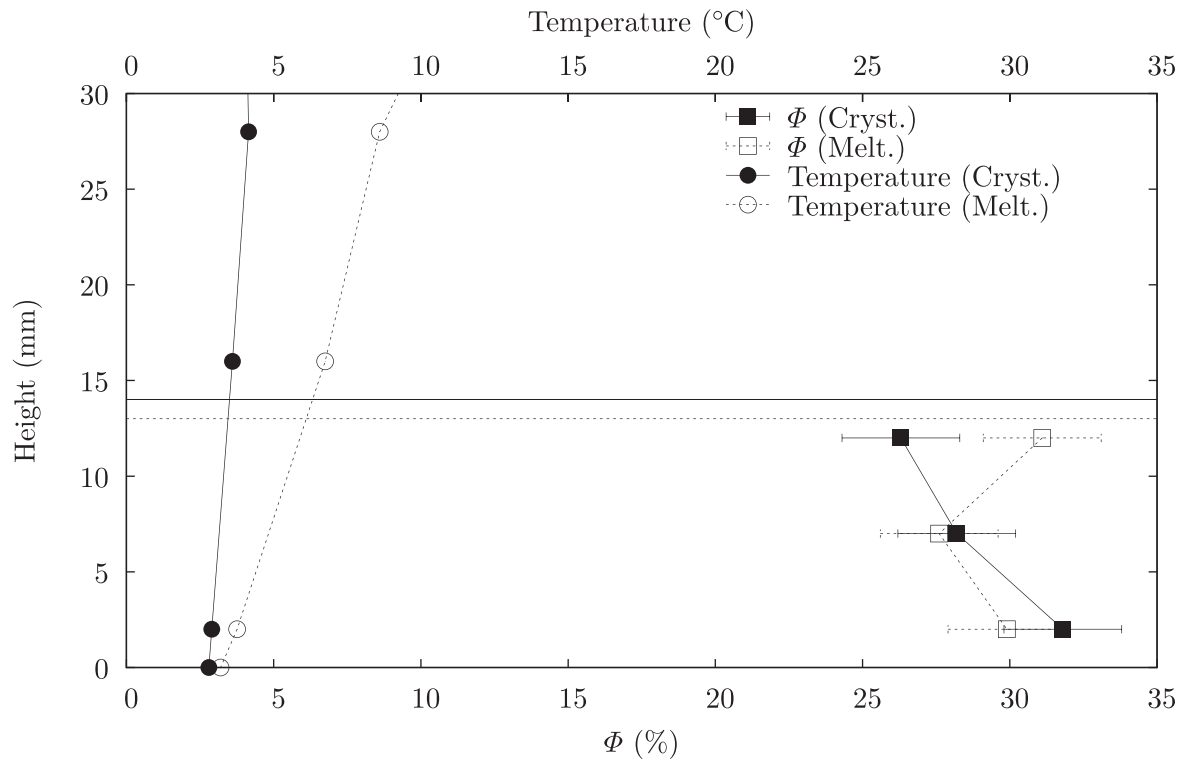


**Figure 12.** Solid fraction (squares) and temperature (circles) profile for melting (dashed) and solidification (solid) experiments at their ends. The dashed lines represent the thickness of the mushy layer for melting (dashed) and solidification (solid) experiments respectively. The prescribed temperature is 3 °C for both experiments.

To track the effects of melting on the mushy layer, we use resistance measurements to determine the solid fraction profile in the mush, at three different heights, 2, 7 and 12 mm above the cold bottom boundary, see Fig. 12. This technique has been suggested by Shirtcliffe *et al.* (1991) and consists in measuring the resistance between two parallel platinum wires a few millimetres apart. Assuming that the solid phase is insulating and thermodynamic equilibrium is reached, we use Archie's empirical law which connects the porosity ( $1 - \Phi$ ) to this resistance  $R_{\text{mush}}$ . Having previously measured the resistance  $R_{\text{liq}}$  in the pure liquid phase at the same temperature and composition, Archie's law takes the following form (Archie 1942; Chiareli & Worster 1992; Shirtcliffe & Kerr 1992; Jahrling & Tait 1996)

$$1 - \Phi = \left( \frac{R_{\text{liq}}}{R_{\text{mush}}} \right)^{1/m}, \quad (2)$$

where  $m$  is an exponent which depends on the tortuosity and is equal to 1.72 (Shirtcliffe & Kerr 1992; Jahrling & Tait 1996). Fig. 12

shows temperature and solid fraction profiles in melting (green) and solidification (red) experiments at 13 g at the end of the experiments. In the solidification experiment, the solid fraction decreases with height, which is consistent with the study of Chen & Chen (1991). The melting from above produces an increase of solid fraction just below the interface, whereas the rest of the solid fraction profile is unchanged. The mean solid fraction predicted by eq. (1) for the solidification experiment is about 29 per cent, that is in agreement with the solid fraction measured by the platinum wires.

### 3.5 Attenuation measurements in a mushy layer

We have used ultrasounds to quantify structural changes in the mush from measurements of attenuation or scattering. During wave propagation, seismic energy is dissipated through absorption or scattering. The absorption is due to anelastic properties of the medium (i.e. seismic energy can be converted to heat). The scattering depends on the geometric arrangement of the medium and is

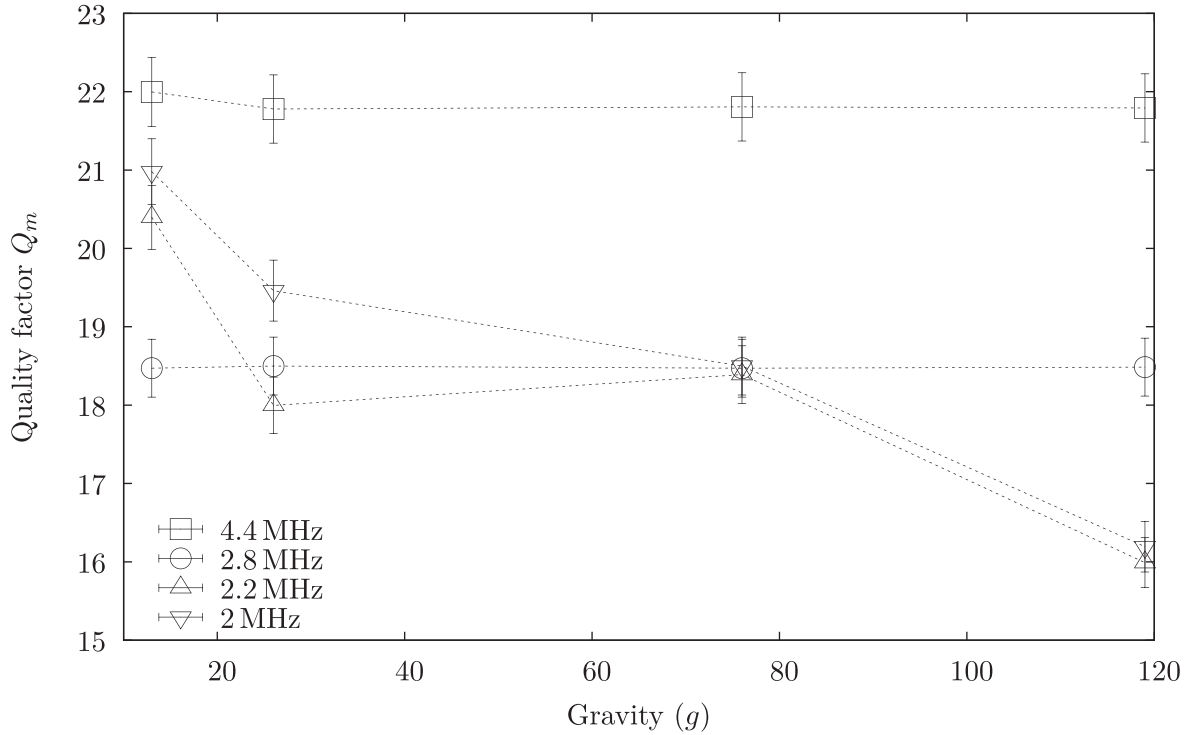


Figure 13. Quality factor  $Q_m$  of the mush as a function of gravity for four different frequencies.

wavelength-dependent, that is, controlled by the ratio of the size of the heterogeneities to the wavelength. The attenuation  $q$  is written as

$$q = \frac{1}{Q_{\text{absorption}}} + \frac{1}{Q_{\text{scattering}}} \quad (3)$$

where  $Q$  is the quality factor. In a two-phase region, elastic energy can also be converted into latent heat with a net contribution to  $Q_{\text{absorption}}$  due to irreversible heat conduction. The wavelength used in this study is close to the length scale of the heterogeneities. Then, we assume that  $Q_{\text{absorption}}$  is negligible compared to  $Q_{\text{scattering}}$ . We use two different methods to measure the attenuation in the mushy layer. The first one is the spectral ratio method (Jordan & Sipkin 1977; Sipkin & Jordan 1980; Romanowicz & Mitchell 2007) and is applied on the transverse signals (PKIKP like, (2) in Fig. 3). In our case, we compared in a frequency domain the spectrum of waves travelling through the liquid to the spectrum of waves travelling through the mushy layer. The spectral ratio is written

$$\ln\left(\frac{A_m}{A_l}\right) = \frac{\pi x f}{c} \left( \frac{1}{Q_l} - \frac{1}{Q_m} \right), \quad (4)$$

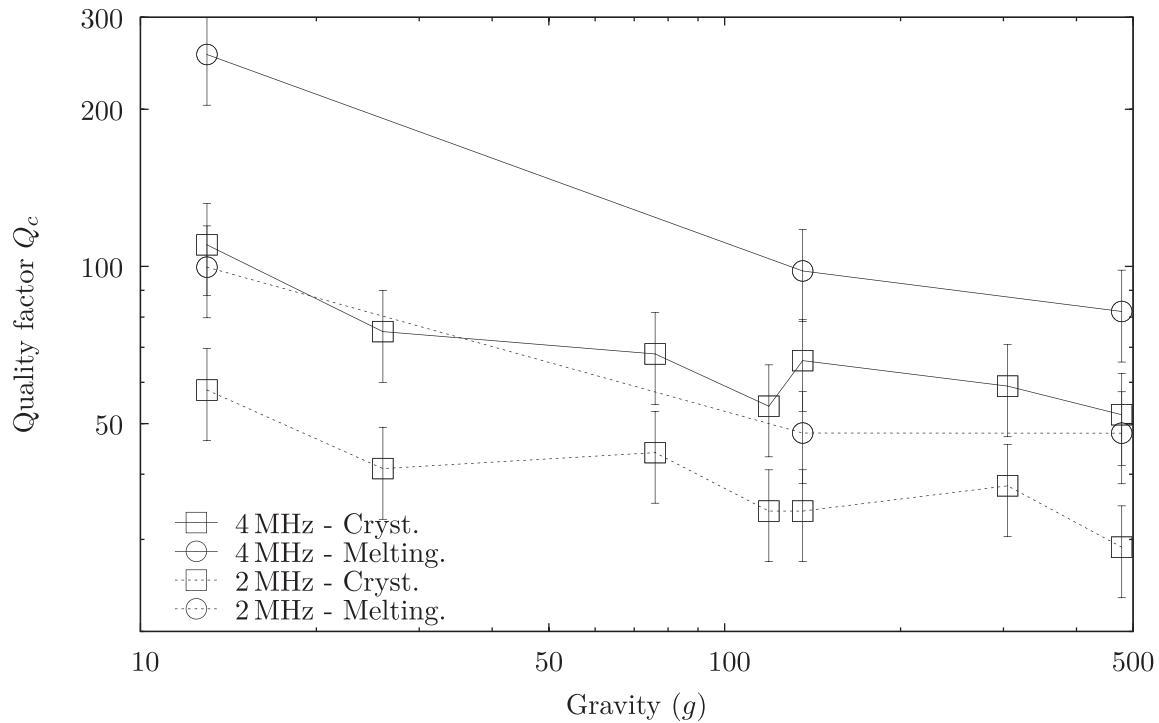
where  $A_l$  and  $A_m$  are spectral amplitudes through the liquid and through the mush, respectively,  $x$  is the distance between the two ultrasonic probes,  $c$  is the wave speed,  $f$  is the frequency, and  $Q_l$  and  $Q_m$  are quality factors of the liquid and of the mush.  $Q_l$  is determined from the spectral ratio of the spectrum of the wave travelling one time and three times in the liquid ( $200 < Q_l < 400$ ). The size of the window is 2  $\mu$ s around the maximum of the signal which corresponds to the arrival time. The quality factor  $Q_m$  is quasi-independent of this windows size. The error of  $Q_m$  is due to the velocity which is measured in the liquid above the mushy layer during the experiments. The velocity error is estimated to be about 2 per cent.

Fig. 13 presents our measurements of attenuation at different gravities, under the condition that the mush is thicker than the size of the ultrasonic probes (15 mm). Between 2.8 and 6 MHz,  $Q_m$  is independent of gravity but its significance is questionable since the signal is largely back-scattered and attenuated, and probably within noise level. For smaller frequencies ( $< 2.5$  MHz), the quality factor decreases with gravity level (Fig. 13), that is, the attenuation increases when the microstructure of the mushy layer changes—solid fraction increasing, interdendritic spacing decreasing and grain sizes decreasing. The waves travelling through the mushy layer are broadened and attenuated and are not followed by a coda, which is consistent with the model predictions of Cormier (2007) for a signal sent perpendicularly to a vertically oriented structure (like a mushy layer).

The second method measures the exponential decrease in the coda of the vertical signals (PKIKP like, (3) in Fig. 3; Aki & Chouet 1975). The quality factor of the coda  $Q_c$  is written as

$$E(f, t) = S(f) t^{-\alpha} e^{-\frac{2\pi f t}{Q_c}} \quad (5)$$

where  $E$  is the power spectral density,  $S$  is the source term and  $\alpha$  is a positive coefficient, usually equal to 2 (Aki & Chouet 1975). The quality factor  $Q_c$  is based on the signal averaged over the last 15 min of the melting or solidification experiments (Fig. 6) when the thickness of the mushy layer is almost constant. In Fig. 6, the error bars denote the standard deviation which is due to the noise level in the ultrasonic signal. For all frequencies,  $Q_c$  decreases with gravity (Fig. 14). Moreover, it is observed that  $Q_c$  is greater when the top of the mushy layer is melted. However, the amplitude of  $Q_c$  depends on the duration of the time windows which prevents a direct comparison with the  $Q_m$  value. The presence of a coda in our signal is consistent with the model of Cormier (2007) for a signal reflected on a heterogeneous medium.



**Figure 14.** Quality factor  $Q_c$  as function of gravity for two different frequencies (2 MHz in dotted lines and 4 MHz in solid lines) during melting (circles) and solidification (squares) experiments.

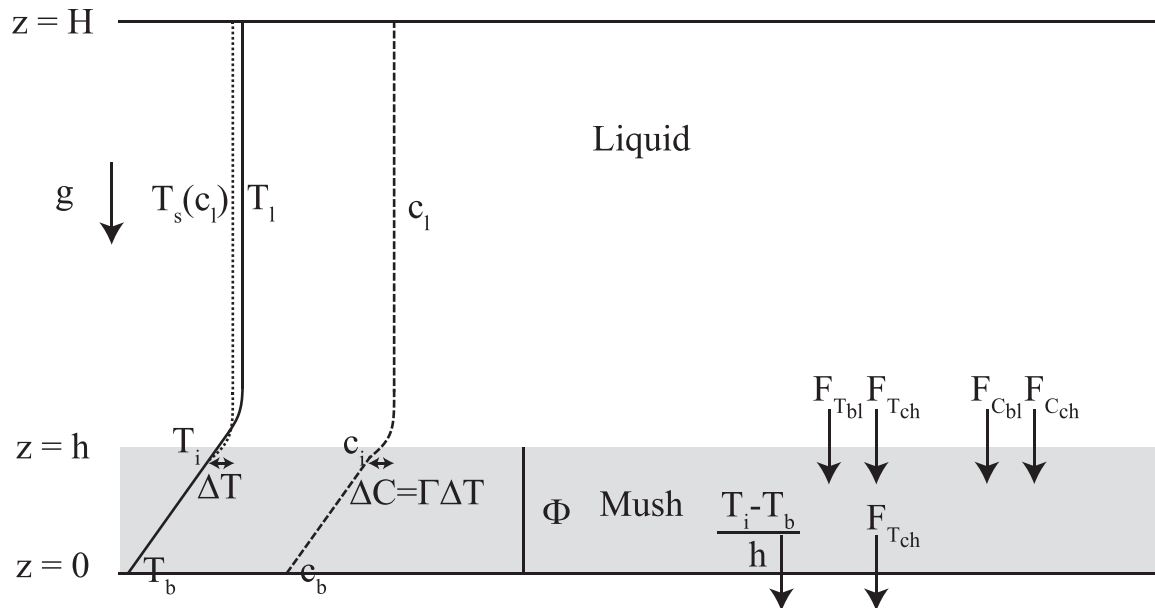


**Figure 15.** Schematic diagram of the model. A mushy layer develops after decreasing the bottom temperature to  $T_b$  from a melt at temperature and concentration  $T_l$  and  $c_l$ , respectively. The solid fraction of the mush is assumed constant and uniform.  $F_T$  and  $F_C$  are heat and solute fluxes between the liquid and mushy layers. The suffix *bl* and *ch* denote the flux due to the boundary layer convection mode or to the mushy layer convection mode respectively.

#### 4 GROWTH MODEL OF THE MUSHY LAYER

A number of models describe the macroscopic evolution of a crystallizing mush (Woods & Huppert 1989; Huppert 1990; Worster 1991; Worster & Kerr 1994; Peppin *et al.* 2008; Wells *et al.* 2010, 2011, 2013; Rees Jones & Worster 2013); the evolution of the thickness  $h$  and the solid fraction  $\Phi$  in the mushy layer, and the (uniform) temperature and concentration in the liquid and at the interface. Fig. 15

shows a sketch of a model where a solution at initial composition  $c_0$  and temperature  $T_0$  is cooled from below at the temperature  $T_b$ . The mushy layer grows in the direction opposite to the gravity. We assume that the liquid convects vigorously, and that the temperature  $T_l$  and concentration  $c_l$  are homogeneous. The temperature and the concentration at the interface are  $T_i$  and  $c_i$ . We assume a uniform (but time-dependent) solid fraction in the mushy layer. The bulk of the mush is assumed to be locally at thermodynamic equilibrium, but disequilibrium is allowed at the mush-liquid interface.

**Table 1.** Physical property values used in the theoretical calculations. The  $\text{NH}_4\text{Cl}$  column is related to our experiments (<sup>a</sup> from Worster & Kerr (1994) and Peppin *et al.* (2008)) while the ‘Inner core’ column shows typical values for numerical modelling relevant to the inner core (<sup>b</sup> from Pozzo *et al.* (2012) and Buffett *et al.* (1996), and <sup>c</sup> from Lum (1996)).

Quantity	Symbol	$\text{NH}_4\text{Cl}^a$	Inner core <sup>b</sup>	Unit
Specific heat of the liquid	$C_{pl}$	3504.8	715	$\text{J kg}^{-1} \text{K}^{-1}$
Specific heat of the solid	$C_{ps}$	1520	715	$\text{J kg}^{-1} \text{K}^{-1}$
Thermal conductivity of the liquid	$k_l$	0.54	150	$\text{W m}^{-1} \text{K}^{-1}$
Thermal conductivity of the solid	$k_s$	2.2	150	$\text{W m}^{-1} \text{K}^{-1}$
Latent heat of crystallization	$L$	$2.81 \times 10^5$	$6 \times 10^5$	$\text{J kg}^{-1}$
Density of the liquid	$\rho_l$	1050	$10^4$	$\text{kg m}^{-3}$
Density of the solid	$\rho_s$	1520	$10^4$	$\text{kg m}^{-3}$
Thermal diffusivity of the liquid	$\kappa_l$	$1.47 \times 10^{-7}$	$2.1 \times 10^{-5}$	$\text{m}^2 \text{s}^{-1}$
Solute diffusivity of the liquid	$D$	$10^{-9}$	$10^{-9}$	$\text{m}^2 \text{s}^{-1}$
Liquidus slope	$\Gamma$	4.79	$10^2$	$^\circ\text{C wt per cent}^{-1}$
Eutectic temperature	$T_e$	-15.9		$^\circ\text{C}$
Eutectic composition	$c_e$	19.7		wt per cent
Kinetic growth parameter	$\mathcal{G}$	$4.14 \times 10^{-7}$	$6 \times 10^{-4}$ <sup>c</sup>	$\text{ms}^{-1} \text{ } ^\circ\text{C}^{-2}$
Initial composition of the liquid	$c_0$	30	90	wt per cent
Height of the cell	$H$	0.07	$3 \times 10^6$	m
Solidification temperature at $c_0$	$T_s(c_0)$	34.57	5100	$^\circ\text{C}$
Bottom temperature	$T_B$	5	5000	$^\circ\text{C}$
Dynamic viscosity	$\nu$	$0.93 \times 10^{-6}$	$10^{-7}$	$\text{m}^2 \text{s}^{-1}$
Solute expansion coefficient	$\beta$	$2.3 \times 10^{-3}$	$10^{-2}$	$\text{wt per cent}^{-1}$
Thermal expansion coefficient	$\alpha$	$3.1 \times 10^{-4}$	$10^{-5}$	$\text{K}^{-1}$

The solidification velocity depends on the supercooling at the interface which corresponds to a difference between the interface  $T_i$  and equilibrium temperature  $T_s(c_l)$ . This under-cooling is of kinetic origin, that is, corresponds to the disequilibrium necessary for the mush to grow. The kinetic growth law is written (Kirkpatrick *et al.* 1976; Worster *et al.* 1990, 1993; Worster & Kerr 1994)

$$\dot{h} = \mathcal{G}(T_s(c_l) - T_i)^2 = \mathcal{G}\Delta T_k^2 \quad (6)$$

where  $\mathcal{G} = 4.14 \times 10^{-7} \text{ m s}^{-1} \text{ } ^\circ\text{C}^{-2}$  a parameter found experimentally by Worster & Kerr (1994), which relates solidification velocity and kinetic undercooling, and is poorly known (Chan *et al.* 1976; Worster & Kerr 1994; Blackmore *et al.* 1997; Peppin *et al.* 2008; Whiteoak *et al.* 2008). In Table 1, we define all parameters used in our model.

#### 4.1 Early height evolution

During the first 15 min, the thickness evolution is independent of gravity (Fig. 16). Hence convection plays a minor role at the beginning. The heat diffusion equation in the cell is written

$$\frac{\partial T}{\partial t} = \kappa \frac{\partial^2 T}{\partial x^2} \quad (7)$$

where  $T$  is the temperature,  $t$  is time,  $x$  is the vertical position and  $\kappa$  is the thermal diffusivity. At the beginning, the solid fraction is small, we then assume the same thermal diffusivity in the mush and in the liquid, and we neglect the latent heat, which is released during solidification. The solution of this equation, when the temperature at the bottom decreases as  $T(t) = ct$ , is (Carslaw & Jaeger 1986)

$$T(t, x) = ct \left[ \left( 1 + \frac{x^2}{2\kappa_l t} \right) \text{erfc} \left( \frac{x}{2\sqrt{\kappa_l t}} \right) - \frac{x}{\sqrt{\pi\kappa_l t}} \exp \left( -\frac{x^2}{4\kappa_l t} \right) \right]. \quad (8)$$

Assuming that the temperature of solidification is constant, the height of the mush is determined by the position at which this temperature is obtained, which is computed numerically (solid line in Fig. 16). However, the mushy layer growth imposes a kinetic under-cooling, which produces a delay of crystallization. Choosing

a supercooling value  $\Delta T_k$  to fit the data we get  $\Delta T_k = 7^\circ\text{C}$ . This is in agreement with the measurements of temperature, on which we have observed a change of slope  $7^\circ\text{C}$  below the initial solidification temperature (arrow in Fig. 5).

#### 4.2 Model of the growth of the mushy layer

A specific feature of our model is that kinetic under-cooling is taken into account. The other ingredients are based on heat and mass conservation. The mushy layer growth is controlled by the heat and solute flux due to boundary layer convection ( $F_{T_{bl}}$  and  $F_{C_{bl}}$ ) and mushy layer convection when super-critical conditions are met ( $F_{T_{ch}}$  and  $F_{C_{ch}}$ ). In the liquid, heat and solute conservation equations are written

$$\left( \frac{M_{\text{tot}}}{\mathcal{A}} - \bar{\rho}h \right) \dot{c}_l = -F_{C_{bl}} - F_{C_{ch}} \quad (9)$$

and

$$C_{pl} \left( \frac{M_{\text{tot}}}{\mathcal{A}} - \bar{\rho}h \right) \dot{T}_l = -F_{T_{bl}} - F_{T_{ch}} - F_p^{\text{liquid}}, \quad (10)$$

where  $M_{\text{tot}}$  is the initial mass of the solution,  $\mathcal{A}$  is the cross-section area,  $\bar{\rho}$  is the mean density of the mush and  $C_{pl}$  is the liquid heat capacity.  $F_p^{\text{liquid}}$  is the heat flux lost through the walls in the liquid due to the poor thermal insulation. Mean quantities in the mush are given by

$$\bar{x} = (1 - \Phi)x_l + \Phi x_s, \quad (11)$$

where  $x$  can be the density, the heat capacity or the thermal conductivity and  $\Phi$  is the solid fraction in the mushy layer.

For the boundary-layer mode of convection, we use classical scaling laws for the fluxes based on the theory of boundary layer stability. We can write the boundary layer flux as proportional to  $Ra^{\frac{1}{3}}$ , with  $Ra$  the Rayleigh number (Woods & Huppert 1989; Worster & Kerr 1994), giving

$$F_{C_{bl}} = 2^{\frac{4}{3}}(1 - \Phi)\rho_l\lambda D \left( \frac{\beta g}{D\nu} \right)^{\frac{1}{3}} (c_l - c_i)^{\frac{4}{3}}, \quad (12)$$

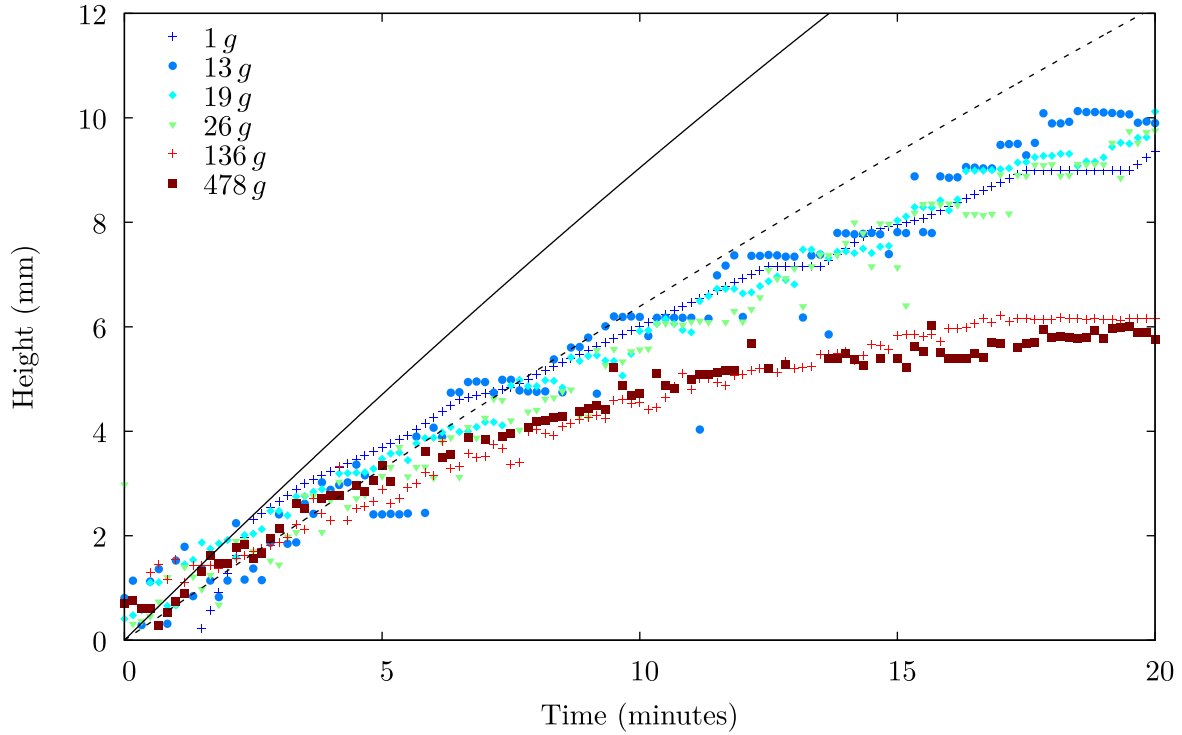


**Figure 16.** Focus on the first 20 min of the height of the mushy layer for different apparent gravities. The black line is the thickness evolution for a conductive model without undercooling (solid) and with a kinetic undercooling  $\Delta T_k = 7^\circ\text{C}$  (dashed line). (For interpretation of the references to colour in this figure legend, the reader is referred to the web version of this paper.)

where  $D$  is solute diffusion,  $\beta$  is a solute expansion coefficient,  $\nu$  is the liquid viscosity,  $c_i$  is the interface concentration, and  $\rho_l$  is the density of the liquid. We assume that this density is constant during the experiment.  $\lambda$  is a constant which depends on the buoyancy ratio (Turner 1979; Worster & Kerr 1994). The factor  $(1 - \Phi)$  corresponds to the fraction of the surface area where the composition difference  $c_l - c_i$  is relevant, i.e., where the bulk liquid is facing the interdendritic liquid. Where the liquid is in contact with the solid phase, Stefan's condition of an imposed composition flux holds, leading to a much smaller value than that with the interdendritic liquid. Assuming heat is transported along with compositional convection as a passive tracer, the heat flux  $F_{T_{bl}}$  is written

$$F_{T_{bl}} = AC_{pl} \left( \frac{T_l - T_i}{c_l - c_i} \right) F_{C_{bl}}, \quad (13)$$

where  $A$  is a constant which depends on the ratio of heat to solute diffusivity (Huppert 1990).

Mushy layer convection is controlled by the mushy layer Rayleigh number  $R_m$  (Wells *et al.* 2010, 2011, 2013; Rees Jones & Worster 2013) written as

$$R_m = \frac{\beta^*(c_i - c_b)g\Pi(\Phi)h}{\nu\kappa_l}, \quad (14)$$

with  $\beta^* = \beta - \Gamma\alpha$  the expansion coefficient due to temperature and concentration changes. The permeability  $\Pi(\Phi)$  depends on the solid fraction as (Tait & Jaupart 1992)

$$\Pi(\Phi) = \frac{\lambda^2}{32} (-2\ln\Phi - \Phi^2 + 4\Phi - 3). \quad (15)$$

The convective solute flux in the mush is given by (Wells *et al.* 2011; Rees Jones & Worster 2013)

$$F_{C_{ch}} = \gamma\kappa_l\rho_l \left( \frac{c_i - c_b}{h} \right) (R_m - R_c), \quad (16)$$

with  $R_c = 25$  the critical Rayleigh number and determined experimentally by Tait & Jaupart (1992). Similarly to the boundary layer heat flux  $F_{T_{bl}}$ , we assume that the velocity field is due to compositional convection alone and the convective heat flux is (Wells *et al.* 2011; Rees Jones & Worster 2013)

$$F_{T_{ch}} = \gamma\kappa_l \left( \frac{T_i - T_b}{h} \right) (R_m - R_c). \quad (17)$$

The parameter  $\gamma$  is determined experimentally by Wells *et al.* (2011) for small  $C$ , the ratio of the difference between the concentration of solid and liquid phases (Worster 1991) and the typical variations of concentration in the liquid

$$C = \frac{c_s - c_0}{c_0 - c_B}. \quad (18)$$

where  $c_s = 1$  is the solid concentration and  $c_B$  is the concentration at the target temperature  $T_B$  at the bottom of the cell ( $5^\circ\text{C}$ ). However in our case, this ratio is large ( $C=11.8$ ). Then  $\gamma$  will be a parameter to determine with our experimental results.

Assuming a constant profile of solid fraction in the mushy layer, we write the global solute and heat conservation

$$\left( \frac{M_{\text{tot}}}{\mathcal{A}} - \bar{\rho}h \right) c_l + \langle \bar{\rho}c \rangle h = \frac{M_{\text{tot}}}{\mathcal{A}} c_0 \quad (19)$$

and

$$\begin{aligned} \frac{\partial}{\partial t} \left[ \left( \frac{M_{\text{tot}}}{\mathcal{A}} - \bar{\rho}h \right) C_{pl}T_l + \overline{\rho C_p h} \langle T \rangle \right] \\ = -\bar{k} \frac{\partial T}{\partial z} \Big|_{\text{bottom}} + \rho_s L \frac{\partial h}{\partial t} - (F_p^{\text{liquid}} + F_p^{\text{mush}}), \end{aligned} \quad (20)$$

where  $\rho_s$  is the density of solid.  $F_p^{\text{mush}}$  and  $F_p^{\text{liquid}}$  are the heat flux lost through the walls in the mushy layer and in the liquid, respectively.

The heat flux extracted by the Peltier device at the bottom of the cell is equal to the sum of the convective (chimney) part (eq. 17) and of the conductive contribution along the liquidus gradient

$$\bar{k} \frac{\partial T}{\partial z} \Big|_{\text{bottom}} = \bar{k} \frac{T_i - T_b}{h} + F_{T_{ch}}. \quad (21)$$

The chimneys contribution  $F_{T_{ch}}$  is included in the bottom heat flux because it corresponds to a global mode of convection in the mush (of uniform permeability in our model). Hence, this mode is capable of changing the temperature profile in the mush and in particular at the bottom in a thermal boundary layer. Its contribution comes in addition to the pure conduction term.

$\langle \bar{\rho}c \rangle$  and  $\langle T \rangle$  are the mean concentration and temperature in the mushy layer and are given by

$$\langle \bar{\rho}c \rangle = (1 - \Phi) \rho_l \frac{(c_i + c_b)}{2} + \Phi c_s \rho_s \quad (22)$$

and

$$\langle T \rangle = \frac{(T_i + T_b)}{2}. \quad (23)$$

These equations can be made dimensionless using the total height  $H$  and diffusion time  $\tau_k = \frac{H^2}{\kappa_l}$ . The dimensionless temperature and concentration are written

$$\theta = \frac{T - T_s(c_0)}{T_s(c_0) - T_B} = \frac{T - T_s(c_0)}{\Delta T} \quad (24)$$

and

$$\chi = \frac{c - c_0}{c_0 - c_B} = \frac{c - c_0}{\Gamma^{-1} \Delta T}. \quad (25)$$

With this scaling,  $\theta$  is equal to  $\chi$  at all heights in the mush (assuming thermodynamic equilibrium).

Finally, noting time derivatives with an overdot, we write the dimensionless system of equations as

$$\dot{h} = \mu(\chi_l - \theta_l)^2 \quad (26)$$

$$\left(1 - \frac{\bar{\rho}}{\rho_l} h\right) \dot{\chi}_l = -\gamma \frac{\chi_l - \chi_b}{h} (Rh \Pi(\Phi)(\chi_i - \chi_b) - R_c) - Nu_\chi (\chi_l - \chi_i)^{\frac{4}{3}} (1 - \Phi) \quad (27)$$

$$\left(1 - \frac{\bar{\rho}}{\rho_l} h\right) \dot{\theta}_l = -\gamma \frac{\theta_l - \theta_b}{h} (Rh \Pi(\Phi)(\chi_i - \chi_b) - R_c) - Nu^* (\theta_l - \theta_i)(\chi_l - \chi_i)^{\frac{1}{3}} (1 - \Phi) - F_p^{\text{liq}} \quad (28)$$

$$\begin{aligned} \hat{h}\Phi = & \left\{ \left(1 - \frac{\rho_s}{\rho_l}\right) \theta_l + \dot{h} [(\theta) - \theta_l] + h \langle \dot{\theta} \rangle \left[ 1 + \Phi \left( \frac{\rho_s C_{ps}}{\rho_l C_{pl}} - 1 \right) \right] \right. \\ & + \frac{\theta_l - \theta_b}{h} \left( \frac{\bar{k}}{k_l} + \gamma (Rh \Pi(\Phi)(\chi_i - \chi_b) - R_c) \right) \\ & + (F_p^{\text{liq}} + F_p^{\text{mush}}) \left. \right\} \left\{ S \frac{\rho_s}{\rho_l} - \left( \frac{\rho_s C_{ps}}{\rho_l C_{pl}} - 1 \right) \langle \theta \rangle \right. \\ & \left. \left. - \left( 1 - \frac{\rho_s}{\rho_l} \right) \theta_l \right\}^{-1} \end{aligned} \quad (29)$$

$$C \left( \frac{\rho_s}{\rho_l} \right) h \Phi = - \left( 1 - \frac{\bar{\rho}}{\rho_l} h \right) \chi_l - \langle \theta \rangle (h - h \Phi) \quad (30)$$

The system of eqs (26)–(30) introduces six dimensionless numbers:

$$\begin{aligned} \mu &= \mathcal{G} \frac{H \Delta T^2}{\kappa_l}, \quad S = \frac{L}{\Delta T C_{pl}}, \\ Nu_\chi &= 2^{\frac{4}{3}} \lambda \frac{D}{\kappa_l} \left( \frac{\beta g \Delta T H^3}{\Gamma D \nu} \right)^{\frac{1}{3}}, \quad Nu^* = A Nu_\chi, \\ R &= \frac{\beta^* g \Delta T \lambda_1^2 H}{\Gamma \nu \kappa_l}, \quad \text{and } C = \frac{c_s - c_0}{c_0 - c_B}. \end{aligned}$$

$\mu$  is a dimensionless kinetic growth parameter.  $S$  is the Stefan number.  $Nu^*$  and  $Nu_\chi$  are the thermal and solute Nusselt numbers, respectively.  $C$  is the dimensionless solid concentration or the compositional ratio (Worster 1991).

Eq. (30) can be used to obtain  $\Phi h$  when  $t$  tends to infinity, by setting  $\theta$  and  $\chi_l$  to  $-1$ , which are the values for a uniform  $T = 5^\circ\text{C}$  and thermodynamic equilibrium. The value obtained at the final thermal equilibrium depends only on the solid concentration  $c_s$  and the density ratio  $\frac{\rho_s}{\rho_l}$  and is independent from gravity:

$$\Phi h = \frac{1}{\frac{\rho_s}{\rho_l} (1 + C)}. \quad (31)$$

With the parameters of Table 1, the minimal value of mushy layer height is 3.78 mm which corresponds to  $\Phi = 1$ .

The heat flux lost through the perspex walls by the liquid and by the mushy layer cannot be neglected because the thermal insulation is not perfect especially in the centrifuge. The corresponding fluxes are written as

$$\begin{aligned} F_p^{\text{liq}} &= p \frac{4k_p}{k_l} \frac{H^2}{le} (\theta_l - \theta_{\text{ext}})(1 - h) \quad \text{and} \\ F_p^{\text{mush}} &= p \frac{4k_p}{k_l} \frac{H^2}{le} (\langle \theta \rangle - \theta_{\text{ext}})h, \end{aligned} \quad (32)$$

where  $k_p = 0.17 \text{ W m}^{-1} \text{ K}^{-1}$  is the thermal conductivity of perspex,  $l = 0.15$  or  $0.035 \text{ m}$  and  $e = 0.0125$  or  $0.03 \text{ m}$  are the length and the thickness of the wall respectively for the tank or the cell in the centrifuge respectively. The prefactor  $p$  accounts for the contribution of the convective heat transport in the centrifuge, for the exact geometry and for the uncertainty related to the measurement of  $\theta_{\text{ext}}$ . The value of this parameter  $p$  is determined using the temperature fluctuations in the liquid due to the poor thermal regulation in the centrifuge (cf. Fig. 5). For each rotation rate,  $p$  is adjusted so that the temperature fluctuations are equal in the model and in the experimental setup.

### 4.3 Comparison between the model and our the experiments

We have applied our model to the conditions of the experiments carried out at 1, 13, 26 and 478 g. The radius dependence of the gravity is assumed to be not significant on the evolution of mushy layer. Using the parameter values of Table 1 to compute the dimensionless control parameters ( $S = 2.81$ ,  $\mu = 159.7$  and  $C = 11.8$ ) leaves three free parameters that need to be fitted using the experimental results,  $A$ ,  $\lambda$  and  $\gamma$ , which depend on the boundary layer and mushy layer convection. Moreover,  $\lambda_1$  is not well-known and plays an important role to determine when the mushy layer Rayleigh number  $R_m$  becomes supercritical. The main experimental data are the evolution of height and the temperature in the liquid. At 1 g, we know also that convection in the mushy layer begins after 15 min and is always active at the end of experiment. Moreover, we know approximately the interface temperature at the end.

**Table 2.** Dimensionless parameters of the solidification experiments at five different gravity values.

$g$	$Nu^*$	$Nu_\chi$	$R$	$\lambda_1$ ( $\mu\text{m}$ )	$p$
1	15.12	37.80	$2.81 \cdot 10^3$	340	1
13	35.80	89.51	$2.53 \cdot 10^4$	280	0.8
26	44.80	112.02	$3.64 \cdot 10^4$	240	0.7
478	118.23	295.58	$2.28 \cdot 10^5$	140	0.35
1327	166.19	415.47	x	x	x

Based on the experimental results at different gravity value and a prior information on free parameters, we have computed models in the 4-D space ( $A$ ,  $\lambda$ ,  $\gamma$  and  $\lambda_1$ ). To find the best models to fit our experimental data at 1, 13, 26 and 478 g, we have minimized the errors between our model outputs and the experimental results (height, liquid temperature, final solid fraction, time of start of the mushy layer convection and the temperature at the interface (only at 1 g)). Table 2 presents the dimensionless numbers used in the model for a set of parameters:  $A = 0.4$ ,  $\lambda = 0.6$  and  $\gamma = 0.01$ .

Fig. 17 presents the comparison between the model (solid lines) and the experimental results (squares) at 1 g. There is a good agreement between both with  $A = 0.4$ ,  $\lambda = 0.6$ ,  $\gamma = 0.01$  and  $\lambda_1 = 340 \mu\text{m}$ . Concerning temperature at the interface, the experimental value is estimated by linear interpolation of the temperatures of the probes on the side, given the interface position determined by direct visualization. There is a reasonable agreement between that experimental temperature (blue squares) and that provided by the model (blue line). The value of  $A$  is consistent with experiments of double-diffusive convection which suggest that the value is order of unity when  $D/\kappa_l \ll 1$  (Woods & Huppert 1989). Turner (1967) determined the ratio between heat and solute flux in the case of finger salt convection, and found 0.56 (Turner 1979).

**Table 3.** Comparison between the model prediction and the experimental data at 1, 13, 26 and 478 g.  $\int F_{\text{Tot}} dt$  denotes the total heat flux, that is, the sum of right-hand side of eq. (28).

$g$	$h_f$		$\Phi_f$		$\frac{\int F_{T_{bl}} dt}{\int F_{T_{tot}} dt}$	$\frac{\int F_{T_{ch}} dt}{\int F_{T_{tot}} dt}$	$\frac{\int F_p^{liq} dt}{\int F_{T_{tot}} dt}$
	model	exp	model	exp	(per cent)	(per cent)	(per cent)
1	0.38	0.37	0.10	0.05	72.3	5.8	21.9
13	0.30	0.31	0.17	0.14	36.6	6.0	57.4
26	0.23	0.24	0.19	0.17	41.2	9.6	49.2
478	0.13	0.12	0.40	0.40	59.0	24.3	16.7

Using the same set of parameters, we applied the same evolution model to cases corresponding to three experiment which have been carried out in the centrifuge at three different gravities 13, 26 and 478 g. Table 3 summarizes the model predictions and compares them with the experimental data. Our model predicts with a good confidence the final height  $h_f$  and final solid fraction  $\Phi_f$ . There is also a good agreement for the evolution of thickness of mush (Fig. 7). The integrated heat flux  $\int F_{T_{ch}} dt$  is smaller than  $\int F_{T_{bl}} dt$  in all experiments but  $\int F_{T_{ch}} dt$  becomes significant when  $g$  is very large. The integrated heat flux lost through the wall  $\int F_p^{liq} dt$  is not negligible especially in the centrifuge at small rotation rate (Table 3).

## 5 MODEL ANALYSIS

The model of mush (Fig. 15) evolution with kinetic undercooling presented above (equations 26 to 30) is rather complex, with five unknowns and eight dimensionless parameters  $\mu$ ,  $S$ ,  $Nu_\chi$ ,  $Nu^*$ ,  $C$ ,  $\rho_l/\rho_s$ ,  $k_l/k_s$  and  $R$  (and even more when heat flux losses through side-walls are considered). Here, we write a simplified version of this model and analyse the evolution of the mush, depending on the

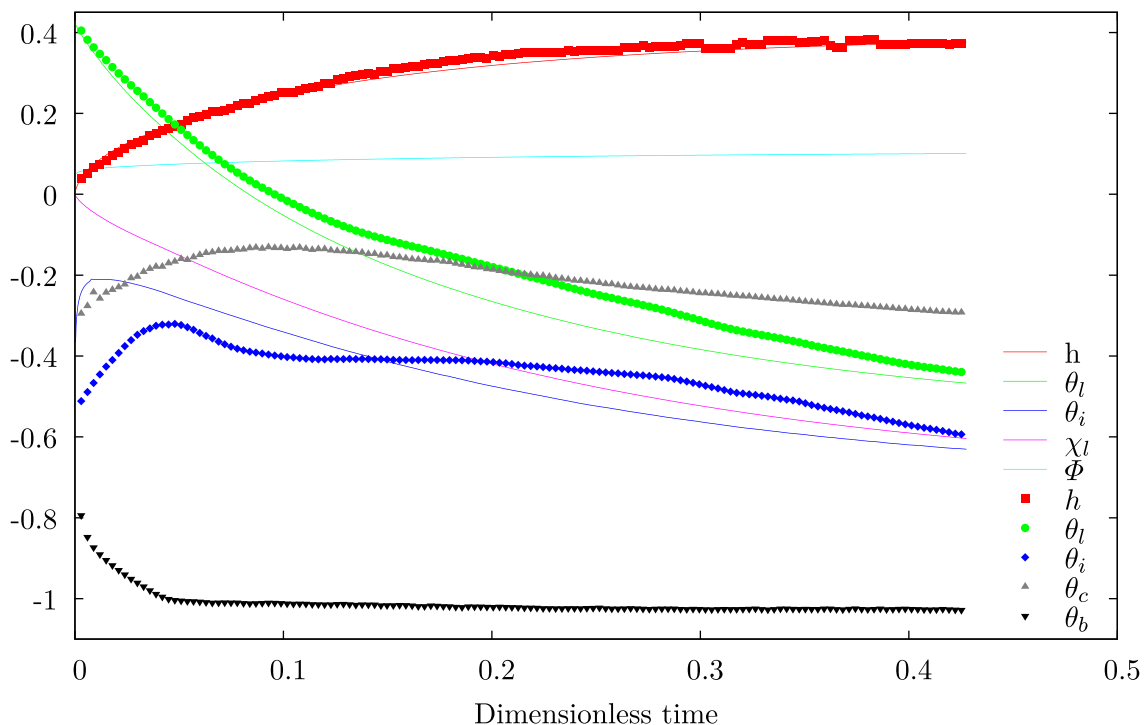


**Figure 17.** Evolution of dimensionless height, temperature, concentration and solid fraction based on the model (solid lines) for  $A = 0.4$ ,  $\lambda = 0.6$ ,  $\gamma = 0.01$  and  $\lambda_1 = 340 \mu\text{m}$ . Different squares denote the experimental results at 1 g. The evolution of interface temperature  $\theta_i$  is obtained by linear interpolation between temperatures probes spaced 1.25 cm (blue squares). (For interpretation of the references to colour in this figure legend, the reader is referred to the web version of this paper.)

values of the dimensionless parameters. The simplifications consist in neglecting the density and conductivity difference between solid and liquid, and in considering an initial condition on the liquidus for the melt. Both Nusselt numbers  $Nu_\chi$  and  $Nu^*$  are supposed to be equal and simply denoted  $Nu$ , thermal and solute chimney fluxes appear to be equal from eqs (26–30), so that  $\theta_l = \chi_l$  at each time, reducing the system to four unknowns. We also restrict the analysis to  $C \gg 1$  and  $S/C \ll 1$ , which are acceptable assumptions for the experiments and geophysical applications. Moreover, it is assumed that the bottom temperature is a Heaviside step function of time, from 0 to  $-1$  (in dimensionless terms) at the onset of crystallization. A final simplifying assumption is made by taking a constant interdendritic spacing in the mush.

With those approximations described above, the governing dimensionless equations for the evolution of the mush can be re-written as follows:

$$0 = (1 - h)\chi_l + Ch\Phi + \frac{\chi_i + \chi_b}{2}h(1 - \Phi), \quad (33)$$

$$\begin{aligned} \frac{\partial}{\partial t} [(1 - h)\chi_l] + \frac{\partial}{\partial t} \left[ \frac{\chi_i + \chi_b}{2}h \right] \\ = -\frac{\chi_i - \chi_b}{h} [1 + \gamma (R\Pi(\Phi)h(\chi_i - \chi_b) - R_c)] + S\frac{\partial h\Phi}{\partial t}, \end{aligned} \quad (34)$$

$$\dot{h} = \mu(\chi_l - \chi_i)^2, \quad (35)$$

$$\begin{aligned} (1 - h)\dot{\chi}_l = -Nu(\chi_l - \chi_i)^{\frac{4}{3}}(1 - \Phi) \\ - \gamma \frac{\chi_i - \chi_b}{h} [R\Pi(\Phi)h(\chi_i - \chi_b) - R_c], \end{aligned} \quad (36)$$

where  $R$  and  $\Pi(\Phi)$  are given by eqs (14) and (15), and  $Nu = 2^{(4/3)}\lambda D\kappa^{-1}(\beta g\Delta TH^3/(\Gamma D\nu))^{(1/3)}$ . The first equation corresponds to the global conservation of ammonium chloride, the second to the heat budget, the third is the kinetic undercooling condition and the last describes solutal exchanges between the mush and liquid layer.

The initial conditions are such that the dimensionless concentration is zero in the liquid  $\chi_l = 0$ . From a specific starting time, we impose a fixed temperature (concentration) at the bottom of the cavity  $\chi_b = -1$ . Initially,  $\chi_i$  must be equal to  $\chi_b = -1$  to avoid an infinite heat transfer (36).

The final state of the system is characterized by a uniform dimensionless temperature  $\chi_l = \chi_i = \chi_b = -1$ . Eq. (33) then leads to the final quantity of solid formed  $h\Phi_\infty$ :

$$h\Phi_\infty = \frac{1}{C+1}. \quad (37)$$

### 5.1 Undercooling kinetic phase

Immediately after the bottom temperature is set to  $-1$ , the bulk liquid composition  $\chi_l$  (and bulk temperature,  $\theta_l = \chi_l$ ) has not changed much ( $\chi_l = 0$ ) and the composition of the first interdendritic liquid is  $\chi_i = -1$ , as discussed above. The undercooling condition allows us to derive the growth rate of the mushy layer,  $\dot{h} = \mu(\chi_l - \chi_i)^2 = \mu$ . So that the first phase of the growing mush is linear in time:

$$h = \mu t, \quad (38)$$

where  $t$  is the time elapsed since the cold temperature has been imposed at the bottom. The interfacial compositional flux condition (36) leads initially to a linear decrease of  $\chi_l$ :

$$\chi_l = -Nu t, \quad (39)$$

as  $\chi_l - \chi_i \simeq 1$  and the mode of convection within the mush has not started yet ( $Rm < R_c$ ). During this initial phase ( $h \ll 1$ ), eq. (33) can be used along with eqs (38) and (39) to evaluate  $h\Phi$ :

$$h\Phi = \frac{\mu + Nu}{\mu(C+1)}h, \quad (40)$$

hence providing the solid fraction  $\Phi$ :

$$\Phi = \frac{\mu + Nu}{\mu(C+1)}. \quad (41)$$

Then eq. (34) can be used to obtain the evolution of  $\chi_i$ :

$$-Nu - \mu = -\frac{\chi_i + 1}{h} + S\frac{\mu + Nu}{\mu(C+1)}\mu, \quad (42)$$

which leads to

$$\chi_i = -1 + \mu(\mu + Nu) \left[ 1 + \frac{S}{C+1} \right] t, \quad (43)$$

At this stage, we only consider the case  $S/C \ll 1$  and  $C \gg 1$ , as this is a reasonable assumption for both our experiments and applications to Earth's inner core. Eq. (43) can be written  $\chi_i = -1 + \mu(\mu + Nu)t$ . This provides us with a timescale for when this first regime must stop, that is, for when  $\chi_i$  approaches zero, as  $\chi_i$  must remain smaller than  $\chi_l$  which will itself be smaller than zero, its initial value. The first regime stops at a typical time  $T_1$  and height  $H_1$ :

$$T_1 = \frac{1}{\mu(\mu + Nu)} \quad H_1 = \frac{1}{(\mu + Nu)}. \quad (44)$$

This must be changed when  $Nu \geq C\mu$ , or the solid fraction (41) would exceed unity. With  $\Phi \simeq 1$ , eq. (33) leads to  $\chi_l = Ch$  (when  $h \ll 1$ ), and (34) to  $\chi_i = -1 + (S + C + 1)\mu^2 t \simeq -1 + C\mu^2 t$ . The duration  $T_{1b}$  and final height  $H_{1b}$  of the undercooling kinetic phase is then:

$$T_{1b} = \frac{1}{\mu^2 C} \quad H_{1b} = \frac{1}{\mu C}. \quad (45)$$

### 5.2 Thermal diffusion regime

Typically, after  $\chi_i$  has changed from  $-1$  to a value close to  $\chi_l$  which is itself still close to zero, we make the assumption that  $\dot{\chi}_i$  plays a negligible role in eq. (34) and check this assumption later. The heat budget eq. (34) can be written:

$$\frac{1}{h} = -\dot{\chi}_l + \frac{\dot{h}}{2} + S\hat{h}\Phi, \quad (46)$$

when  $h$  is still very small compared to unity and convection in the mush not yet effective ( $R_m < R_c$ ). Eq. (33) is used to evaluate  $h\Phi$ :

$$\chi_l + Ch\Phi - \frac{h}{2} = 0, \quad (47)$$

so that eq. (46) can be written as follows:

$$\frac{1}{h} \simeq -\dot{\chi}_l + \frac{\dot{h}}{2}. \quad (48)$$

The conduction heat flux  $1/h$  extracted at the base of the experiment is balanced by cooling the bulk of the fluid  $-\dot{\chi}_l$  or by cooling the mushy layer ( $\dot{h}/2$ ) and the negligible contribution of the latent heat release corresponding to the factor  $S/C$ . The relative importance of these terms is measured, near the end of the first kinetic phase, by  $Nu$  and  $\mu/2$  respectively. Hence the study of the evolution of the system is divided in two cases  $Nu \gg \mu$  and  $Nu \ll \mu$ .

### 5.2.1 $Nu \gg \mu$

The thermal eq. (48) is approximated by

$$\frac{1}{h} = -\dot{\chi}_l = Nu (\chi_l - \chi_i)^{\frac{4}{3}} (1 - \Phi), \quad (49)$$

using the interface condition (36). With the undercooling condition (35), this equation can be written:

$$\frac{1}{h} = Nu \left( \frac{\dot{h}}{\mu} \right)^{\frac{2}{3}} (1 - \Phi). \quad (50)$$

When the solid fraction is small (not very close to unity), this equation takes the form:

$$h \left( \frac{\dot{h}}{\mu} \right)^{\frac{2}{3}} = \frac{1}{Nu}, \quad (51)$$

leading to

$$\frac{h}{H_1} \simeq \left( \frac{t}{T_1} \right)^{\frac{2}{5}}. \quad (52)$$

From (33), we have  $(C + 1/2)\hat{h}\hat{\Phi} = \dot{h}/2 - \dot{\chi}_l$  and with (48) we obtain:

$$C\hat{h}\hat{\Phi} = \frac{1}{h}, \quad (53)$$

which can be integrated to provide  $h\Phi$ :

$$h\Phi \simeq \frac{1}{\mu C} \left( \frac{t}{T_1} \right)^{\frac{3}{5}}, \quad (54)$$

which then, using eq. (52), leads to an expression for the solid fraction  $\Phi$ :

$$\Phi \simeq \frac{Nu}{\mu C} \left( \frac{t}{T_1} \right)^{\frac{1}{5}}, \quad (55)$$

This regime can only exist when  $\Phi \leq 1$  at  $t = T_1$ . This is the case when  $Nu < C\mu$ . Otherwise, when  $\Phi$  is nearly unity, our approximations fail and a new analysis must be done. When  $\Phi \simeq 1$  and  $h \ll 1$ , eq. (33) can be written:

$$\chi_l = -Ch, \quad (56)$$

and eq. (48) leads to:

$$\frac{1}{h} = C\dot{h}. \quad (57)$$

The solution is:

$$\frac{h}{H_{1b}} \sim \left( \frac{t}{T_{1b}} \right)^{\frac{1}{2}}, \quad (58)$$

where  $T_{1b}$  and  $H_{1b}$  are defined in eq. (45). This regime number 1 in the  $Nu$ - $\mu$  diagram on Fig. 18 is typically represented by the case (a) (see also Fig. 19 and Table 4).

When  $Nu < C\mu$ , the  $h \sim t^{1/2}$  regime ends when one of the following conditions is met: either  $h\Phi$  has reached its final value (37), or  $\Phi$  has reached 1. The times when these conditions are met is evaluated from (54) and (55):

$$\frac{T_{2a}}{T_1} = \mu^{\frac{5}{3}}, \quad \frac{T_{2b}}{T_1} = \left( \frac{\mu C}{Nu} \right)^5 \quad (59)$$

Those times coincide when:

$$Nu \sim C\mu^{\frac{2}{3}}, \quad (60)$$

When  $Nu > C\mu^{2/3}$ , the condition  $\Phi = 1$  is met at the time  $T_{2b}$  before the end of the crystallization, hence a phase  $h \sim t^{1/2}$  follows (regime 3, case (c) on Figs 18 and 19, and Table 4). On the contrary, when  $Nu < C\mu^{2/3}$ , crystallization stops before the solid fraction reaches unity, at a time  $T_{2a}$ . In that case, the final height scales as  $\mu^{2/3}/Nu$  (regime 2, case (b) on Figs 18 and 19, and Table 4).

### 5.2.2 $Nu \ll \mu$

Now, in eq. (48) we must retain the term  $\dot{h}$ , which under the same assumption of constant  $\chi_i$ , can be rewritten into:

$$h\dot{h} = 2, \quad (61)$$

with solution

$$\frac{h}{H_1} = \left( \frac{t}{T_1} \right)^{\frac{1}{2}}. \quad (62)$$

Eq. (53) is still valid so that it can be concluded that the solid fraction is a constant  $\Phi \sim 1/C$ , similarly as for the initial undercooling kinetic phase. This regime can stop if  $-\dot{\chi}_l$  becomes larger than  $\dot{h}$  (see eq. 48) or if the total quantity of solid has been produced, that is, when  $h \sim 1$ . This corresponds to the respective times

$$T_{2c} \sim \frac{\mu^4}{Nu^6}, \quad T_{2d} \sim 1. \quad (63)$$

Those times are equal when  $Nu \sim \mu^{2/3}$ . For smaller Nusselt numbers, the crystallization is completed before  $-\dot{\chi}_l$  becomes larger than  $\dot{h}$ , so that there is only a regime with  $h \sim t^{1/2}$ , with a final height of order unity and final solid fraction  $1/C$  (regime 6, case (f) or (g) on Figs 18 and 19, and Table 4). For larger Nusselt numbers, at time  $T_{2c}$ , the  $h \sim t^{1/2}$  regime is changed into a  $h \sim t^{2/5}$ , as in the previous section:

$$\frac{h}{H_{2c}} = \left( \frac{t}{T_{2c}} \right)^{\frac{2}{5}}, \quad (64)$$

where  $H_{2c} = H_1(T_{2c}/T_1)^{1/2}$ . From (53), we obtain  $h\Phi \sim \mu^2/(C\mu^3)(t/T_{2c})^{3/5}$  and  $\Phi \sim 1/C(t/T_{2c})^{1/5}$ . In this last regime, two possibilities exist again: either crystallization is completed before the solid fraction reaches unity, or  $\Phi$  become unity before the end of the process and a final phase takes place with  $h \sim t^{1/2}$  (regime 5, case (e) on Figs 18 and 20, and Table 4). The boundary between these possibilities is found to be:

$$Nu \sim C\mu^{\frac{2}{3}}. \quad (65)$$

In the regime where the solid fraction does not reach unity,  $\mu^{2/3} < Nu < C\mu^{2/3}$ , the final height is found to be of order  $\mu^{2/3}/Nu$  (regime 4, case (d) on Figs 18 and 19, and Table 4).

## 5.3 Convection in the mush

We now consider convection effects within the mush, when buoyancy forces are supercritical  $R\Pi(\Phi)h(\chi_i - \chi_b) > R_c$ , especially when a small solid fraction is expected from the regime analysis of the previous section  $Nu < \mu^{2/3}$ . In geophysical conditions, with a sufficiently large Rayleigh parameter  $R$ , convection in the mush can change a small solid fraction into a solid fraction very close to unity.

With a solid fraction close to unity and  $h \ll 1$ , eq. (33) leads to  $\chi_l = -Ch$ . Eq. (34), with a large dimensionless Rayleigh  $R$ , and

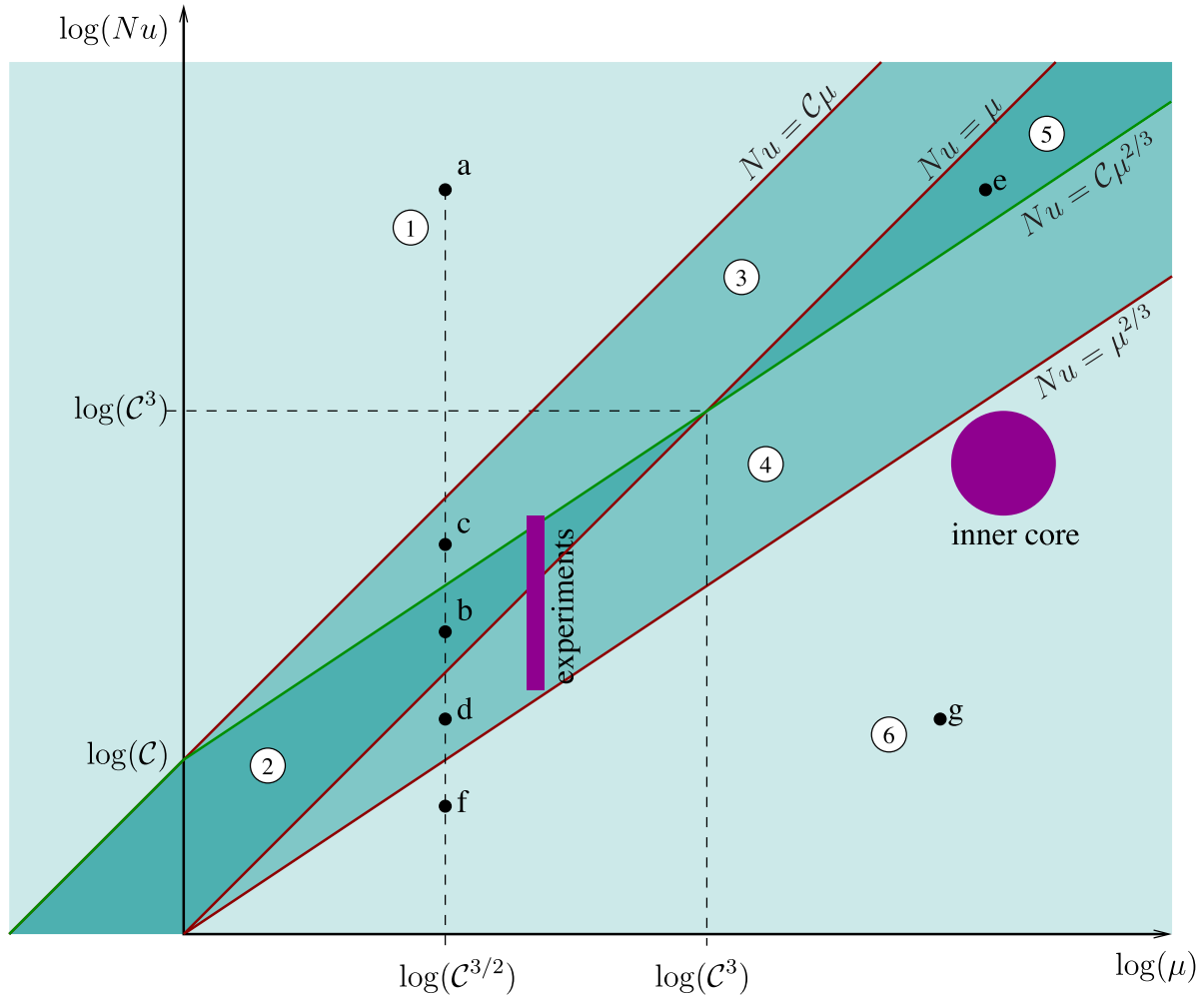


**Figure 18.** Identification of the different regimes of the set of governing equations in the  $Nu-\mu$  space of parameters (ignoring bulk convection within the mush, i.e. small  $R$ ). The characteristics of the different regimes are summarized in Table 4. Above the green line, the solid fraction is of order unity at the end of the crystallization.

$C \gg 1$ , takes the form

$$\left(1 + \frac{S}{C} + \frac{1}{2C}\right) \dot{\chi}_l = -\frac{\chi_i - \chi_b}{h} \times [1 + \gamma (R\Pi(\Phi)h(\chi_i - \chi_b) - R_c)]. \quad (66)$$

This equation has to be compared to the equation of heat transfer between the mush and the liquid (36). If the boundary layer heat transfer can be neglected compared to the contribution of convection in the mush, this equation can be written

$$\dot{\chi}_l = -\gamma \frac{\chi_i - \chi_b}{h} [R\Pi(\Phi)h(\chi_i - \chi_b) - R_c]. \quad (67)$$

It follows from eqs (66) and (67) that the actual Rayleigh number of the mush  $R\Pi(\Phi)h(\chi_i - \chi_b)$  is constrained

$$R\Pi(\Phi)h(\chi_i - \chi_b) = R_c + \frac{C}{\gamma(S + \frac{1}{2})}. \quad (68)$$

What actually happens is that, however large the parameter  $R$  is, the solid fraction becomes close enough to unity, so that the permeability function  $\Pi(\Phi)$  is small enough to bring the Rayleigh number  $R\Pi(\Phi)h(\chi_i - \chi_b)$  just above the critical threshold  $R_c$  by the finite amount given by eq. (68).

In a large time range,  $\chi_i - \chi_b \simeq 1$  so that eq. (67) can be integrated (using eq (68)):

$$h \simeq \sqrt{\frac{2}{S + \frac{1}{2}}} t^{\frac{1}{2}}. \quad (69)$$

A better approximation is obtained, using the approximation  $\chi_i \simeq \chi_l$ . In this case, eq. (67) can be written as

$$C\dot{h} = \frac{1 - Ch}{h} \frac{C}{(S + \frac{1}{2})}, \quad (70)$$

with implicit solution

$$Ch + \ln(1 - Ch) = -\frac{C^2 t}{S + \frac{1}{2}}, \quad (71)$$

for which eq. (69) is an approximation when  $Ch \ll 1$ .

Before that phase of saturated Rayleigh number, when the Rayleigh number goes above the critical value  $R_c$ , there is an intermediate regime where the heat extracted by the convection in the mush is nearly constant:  $\chi_i - \chi_b \simeq 1$ ,  $\Pi(\Phi) \sim 1$ :

$$\dot{\chi}_l \simeq -\gamma R, \quad (72)$$

implying that  $\chi_l$  decreases linearly with time. From eq. (33), we have  $Ch\Phi \simeq -\chi_l$  so that the product  $h\Phi$  increases linearly with time. As

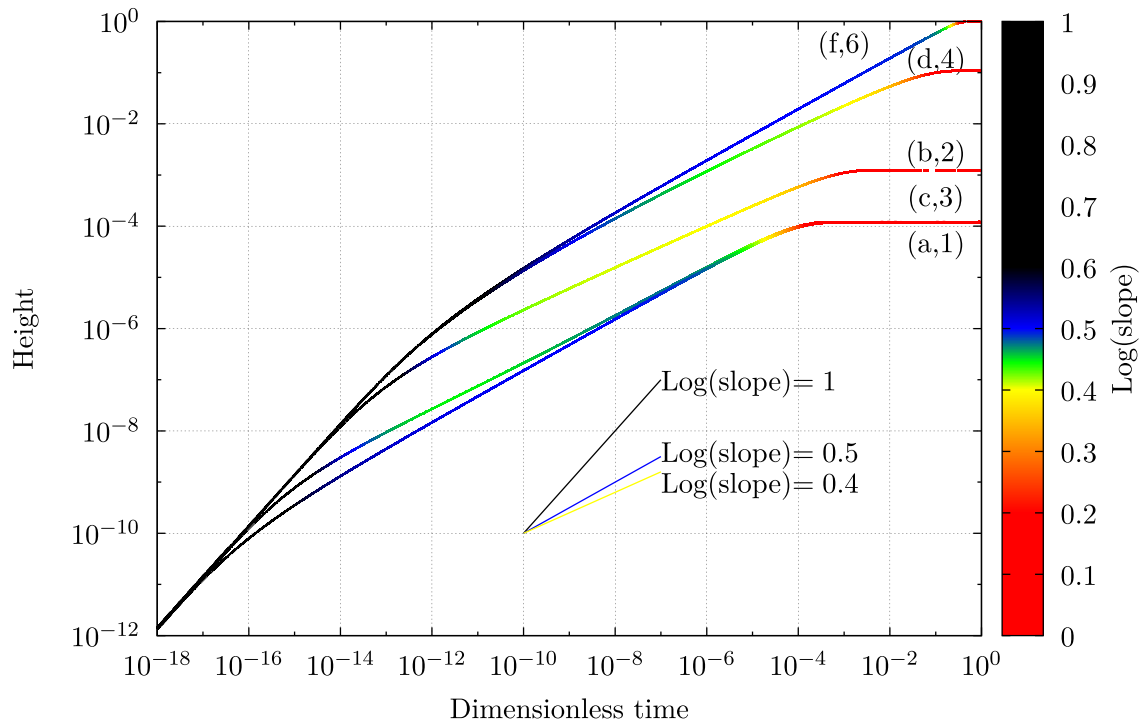


**Figure 19.** Five curves of mush thickness evolution corresponding to the points (a) to (d) and (f) on Fig. 18, in the asymptotic case  $C = 10^4$ ,  $S = 10^2$ ,  $\mu = 10^6$ ,  $Nu = 10^3$  (f),  $10^5$  (d),  $10^7$  (b),  $10^9$  (c) and  $10^{11}$  (a). The slope is plotted in logarithmic colour scale. (For interpretation of the references to colour in this figure legend, the reader is referred to the web version of this paper.)

$h \sim t^{1/2}$  at the end of the previous regime ( $t < 10^{-15}$ , Fig. 21), this leads to  $\Phi \sim t^{1/2}$  ( $10^{-15} < t < 10^{-10}$ ). As  $\chi_l$  is decreasing,  $\chi_l - \chi_i$  decreases as well, hence  $h$  increases has a tendency to increase at a slower pace, so that  $\Phi$  increases slightly faster than  $t^{1/2}$ .

In summary, in this section, the analysis of an idealized system of equations for the evolution of the mush has been carried on in two stages. In a first stage, the evolution of the mush has been studied in the absence of bulk mush convection ( $R = 0$ ), in a 2-D parameter space spanned by the dimensionless numbers  $Nu$  and  $\mu$ . The results of this analysis are summarized in Fig. 18 and Table 4. Both parameters affect the strength of convection in the boundary layer at the top of the mush, in opposite ways. Increasing  $Nu$  enhances heat and mass transfer between the liquid and the mush, resulting in a larger solid fraction in the mush. Alternatively, increasing  $\mu$  amounts to reducing kinetic undercooling (for a given growth rate of the mush), which is the driving temperature difference for convection in the boundary layer. Immediately after a cold temperature is set at the bottom of the crystallization cell, whatever  $Nu$  and  $\mu$ ,

**Table 4.** Description of the evolution and final state of the differential equations modelling mush crystallization, with kinetic undercooling and without convection in the mush.

Number	Height evolution	$h_\infty$	$\Phi_\infty$
1 (a)	$h \simeq \mu t$ then $h \sim t^{1/2}$	$C^{-1}$	1
2 (b)	$h \simeq \mu t$ then $h \sim t^{2/5}$	$\mu^{2/3} Nu^{-1}$	$C^{-1} \mu^{-2/3} Nu$
3 (c)	$h \simeq \mu t$ then $h \sim t^{2/5}$ then $h \sim t^{1/2}$	$C^{-1}$	1
4 (d)	$h \simeq \mu t$ then $h \sim t^{1/2}$ then $h \sim t^{2/5}$	$\mu^{2/3} Nu^{-1}$	$C^{-1} \mu^{-2/3} Nu$
5 (e)	$h \simeq \mu t$ then $h \sim t^{1/2}$ then $h \sim t^{2/5}$ then $h \sim t^{1/2}$	$C^{-1}$	1
6 (f,g)	$h \simeq \mu t$ then $h \sim t^{1/2}$	1	$C^{-1}$

there is a short phase of kinetic undercooling, during which the growth rate of the mush is directly related to the temperature difference between the liquid and the boundary. During this phase, the solid fraction is small in the mush (of order  $C^{-1}$ ). A second phase is dominated by thermal diffusion, during which the growth of the mush is limited by conduction through the mush. This is the starting point for the competition between  $Nu$  and  $\mu$ . When  $Nu \gg \mu$  (regime 1 on Fig. 18), boundary-layer convection is efficient and transfers ‘fresh’ liquid that can crystallize in the mush, increasing solid fraction close to unity. On the contrary, when  $Nu \ll \mu$  (regime 6 on Fig. 18), convective mass transfer is negligible and the solid fraction remains close to  $C^{-1}$ . In an intermediate parameter region (between  $Nu = \mu^{2/3}$  and  $Nu = C\mu$ ), different regimes exist, leading to a final intermediate value for the solid fraction in the mush, between  $C^{-1}$  and 1.

In a second stage, the effect of convection within the mush is considered. Its effect is less important when boundary-layer convection was already able to increase solid fraction close to unity. More importantly, in the regime 6, when  $Nu \ll \mu$ , the effect of the mush convection parameter  $R$  may change completely the fate of the solid fraction in the mush: instead of a small value of order  $C^{-1}$ , bulk convection within the mush can lead to a solid fraction of order unity.

## 6 IMPLICATIONS FOR THE EARTH’S CORE

Many aspects of our experimental setup differ from the conditions of inner core crystallization. Our model is designed for a Cartesian geometry, not spherical. Heat is extracted from below in the model, while it is actually extracted from above for the inner core. However, we can make an attempt to run the model in a range of parameters that would be appropriate for the inner core and observe the resulting mush structure.

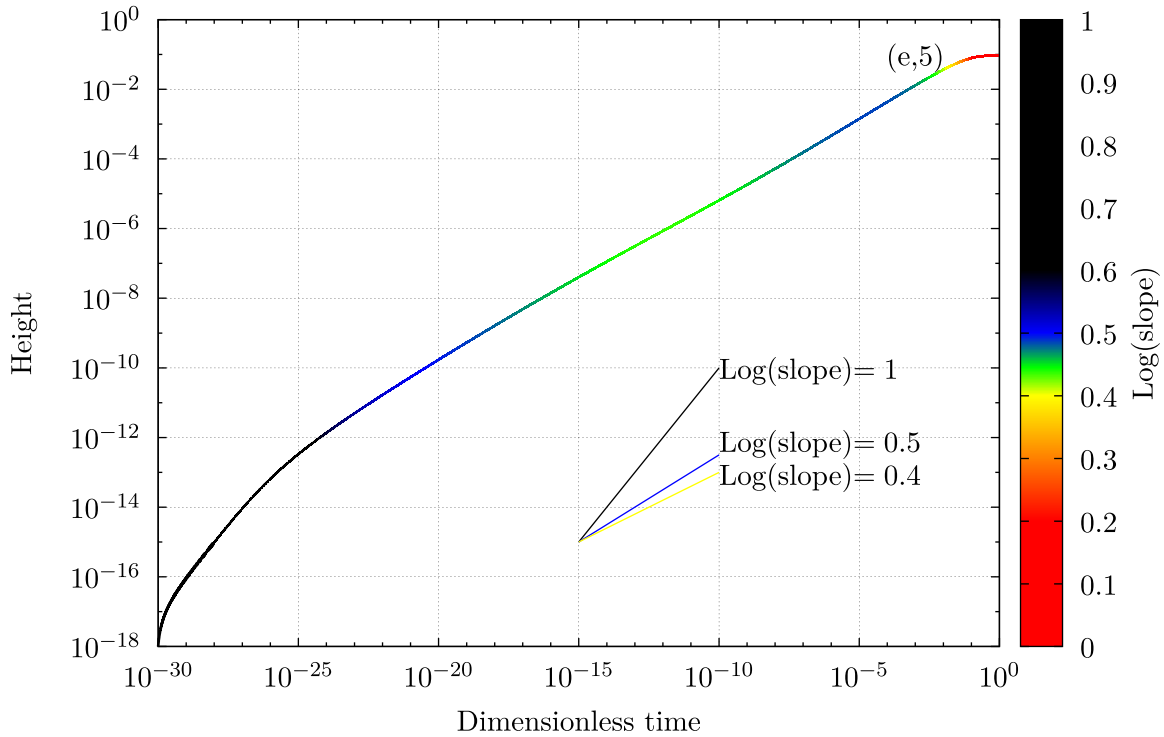


**Figure 20.** Regime 5 computed with  $C = 10$ ,  $S = 1$ ,  $\mu = 10^{13}$ ,  $Nu = 10^{11}$ , cf. Fig. 18(e). Height is plotted while the slope (in logarithmic colour scale) shows that, after the linear phase (slope 1), the slope is around 1/2, decreasing towards 2/5 and increasing again towards 1/2, before the end of the crystallization process. (For interpretation of the references to colour in this figure legend, the reader is referred to the web version of this paper.)

The typical relevant dimensional scales are shown in Table 1. They are not meant to be values at the cutting-edge of our current knowledge, just values of the correct order of magnitude. The liquid core is supposed to be made of 90 per cent iron with light elements. In these parameters, the temperature difference 100 K corresponds to the typical drop of crystallization temperature on the ICB between its origin and the present days. These parameters lead to the following values for the dimensionless quantities playing a role in our mush model:

$$\begin{aligned} \mu &= 8.6 \cdot 10^{11}, & Nu_\chi &= 1.3 \cdot 10^7, & C &= 10, & S &= 8.4, \\ R &= 5.15 \cdot 10^{16}, \end{aligned} \quad (73)$$

obtained for a gravity level of  $4 \text{ m s}^{-2}$  and an interdendritic primary spacing of 1 m (Esbensen & Buchwald 1982; Deguen *et al.* 2007). In the  $Nu-\mu$  parameter space (Fig. 18), these values of  $Nu$  and  $\mu$  put it clearly within regime number 6. As shown in Section 5 (see Fig. 21), boundary layer convection is not very efficient and the solid fraction should remain very low, of order  $\Phi \simeq 0.1$ . However, with a large Rayleigh number in the mush, mush convection is capable of changing it for a solid fraction close to unity (see Fig. 22). Moreover, it can be seen that the Rayleigh number remains close to the expected value,  $Rm \simeq R_c + C/(\gamma(S + 1/2)) \simeq 137$ . It can also be seen that the flux (heat and mass transfer) due to convection in the mush exceeds that due to boundary layer convection by orders of magnitude (Fig. 22).

This application of our mush model to the inner core highlights a crucial difference in regime compared to that of the hypergravity experiments. In these experiments, convection in the mush is certainly present and chimneys are indeed observed, however convection in the mush is not dominant compared to boundary layer convection. It has a moderate impact on the solid fraction (or mush height). On the contrary, for inner core conditions, it is expected that convec-

tion in the mush is the key player and essentially responsible for the expected solid fraction very close to unity. In addition, we have not taken into account the deformation of the solid matrix (Sumita *et al.* 1996), and we can expect a further increase in solid fraction due to compaction.

## 7 DISCUSSION

In this paper, we essentially investigate the opportunity to study crystallization under gravity levels significantly larger than usual on Earth (up to 1300 g). This proves to be a useful tool: other parameters can be varied (size, thermal conditions, ...) and perhaps lead to similar effects, but it is for instance very difficult to change significantly the interdendritic spacing, or mush permeability, so that the effect of convection cannot be changed much under 1 g. This is due to the weak dependence of interdendritic spacing on crystallization rate or thermal gradient. On the contrary, increasing gravity has an immediate linear impact on convection, on the boundary-layer mode above or within the mush. A related observation is that the solid fraction in laboratory experiments using ammonium chloride is always rather small, below 10 per cent. With an enhanced gravity, larger solid fractions can be reached, which may be more relevant to some applications in industry or geophysics.

Hypergravity crystallization experiments can be considered as the (cheap) counterpart of microgravity experiments, where convective effects have been reduced as much as possible (e.g. Dupouy *et al.* 1992; O'Rourke *et al.* 2012). Another possibility (Tait & Jaupart 1992) is to increase the viscosity of the melt with the addition of a polymer. Hypergravity in a centrifuge comes necessarily with Coriolis forces. We have considered that Coriolis forces do not play a major role in the boundary-layer mode or in mush convection. This is justified when the Ekman number, which compares the Coriolis

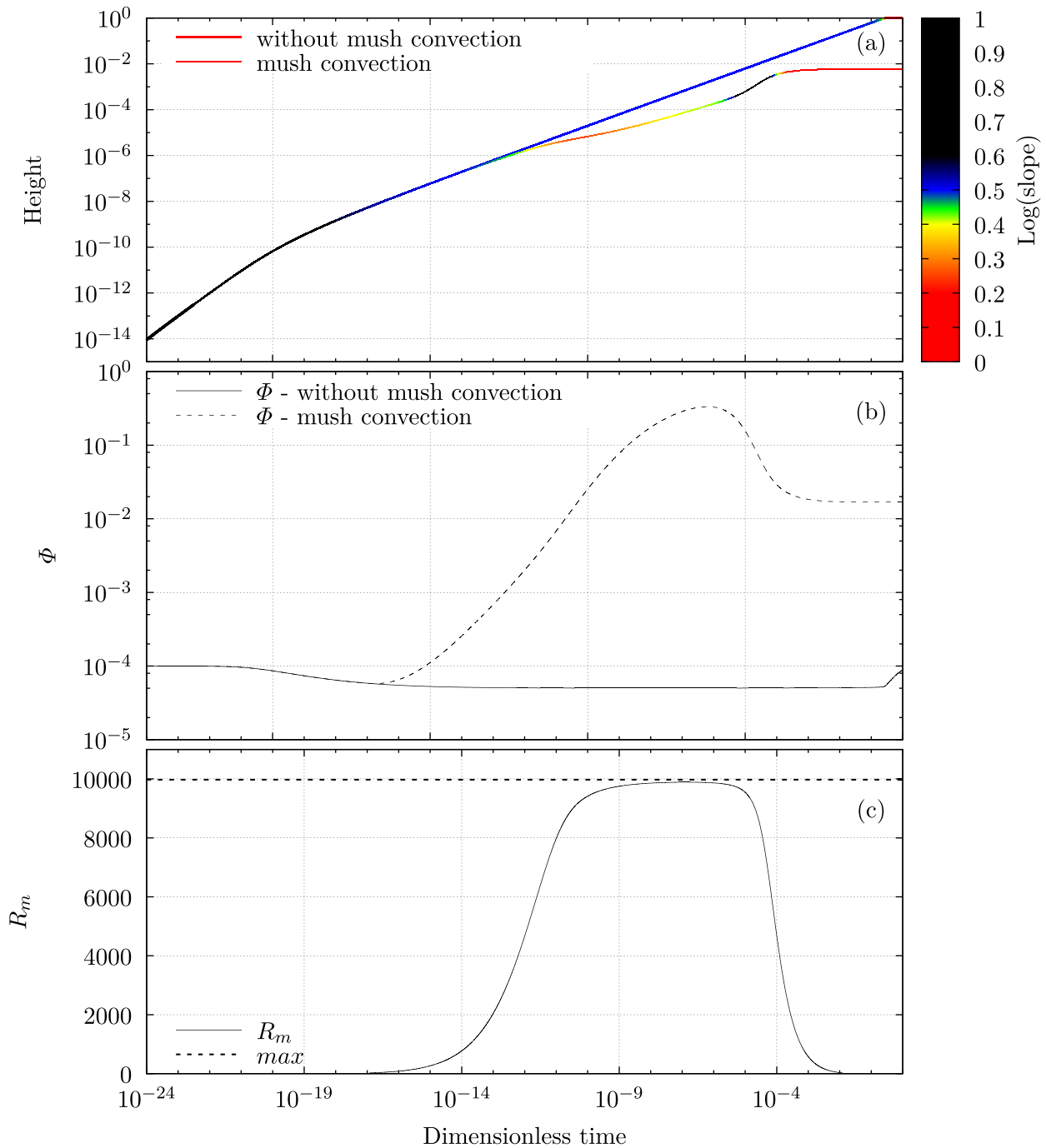


**Figure 21.** Within the regime (6), when a large parameter  $R$  is imposed  $C = 10^4$ ,  $S = 10^2$ ,  $\mu = 10^{10}$ ,  $Nu = 10^5$ ,  $R = 10^{10}$  and  $\gamma = 0.01$ , cf Fig. 18(g). Height (a), solid fraction (b) and mush Rayleigh number (c) are plotted as the solidification proceeds. This is compared to the case without mush convection: same parameters except  $R = 10^{-4}$  (thick line in panel (a) and solid line in panel (b)). In panel (c), the dashed line corresponds to eq. (68). (For interpretation of the references to colour in this figure legend, the reader is referred to the web version of this paper.)

and viscous forces, based on the typical length scale (boundary-layer thickness, dendritic primary arm spacing) is not very small compared to unity.

Regarding the study of the Earth's inner core, our rationale for using hypergravity in a centrifuge was motivated by similar arguments. The timescale and length scale are 1 Gyr and  $10^3$  km with effectively small thermal driving forces as the heat extracted from the inner core is of order 1 TW (or less), corresponding to  $5 \text{ mW m}^{-2}$ . With such parameters, the microstructures of crystallization are presumably metres or larger (Deguen *et al.* 2007). Convection

can act strongly to exchange species between the mush and the liquid outer core. In order to mimic a similar degree of convective effects in a laboratory experiment with submillimetre microstructures, we decided to use the apparent gravity of a laboratory centrifuge.

The results obtained in this paper concern different aspects. The main first order observation is the increase in solid fraction within the mush with increasing gravity levels. This is directly related to the measured thickness of the mush, as each crystallization experiment is run until the same mass of ammonium chloride has been solidified. We have also built a numerical model, based on heat and

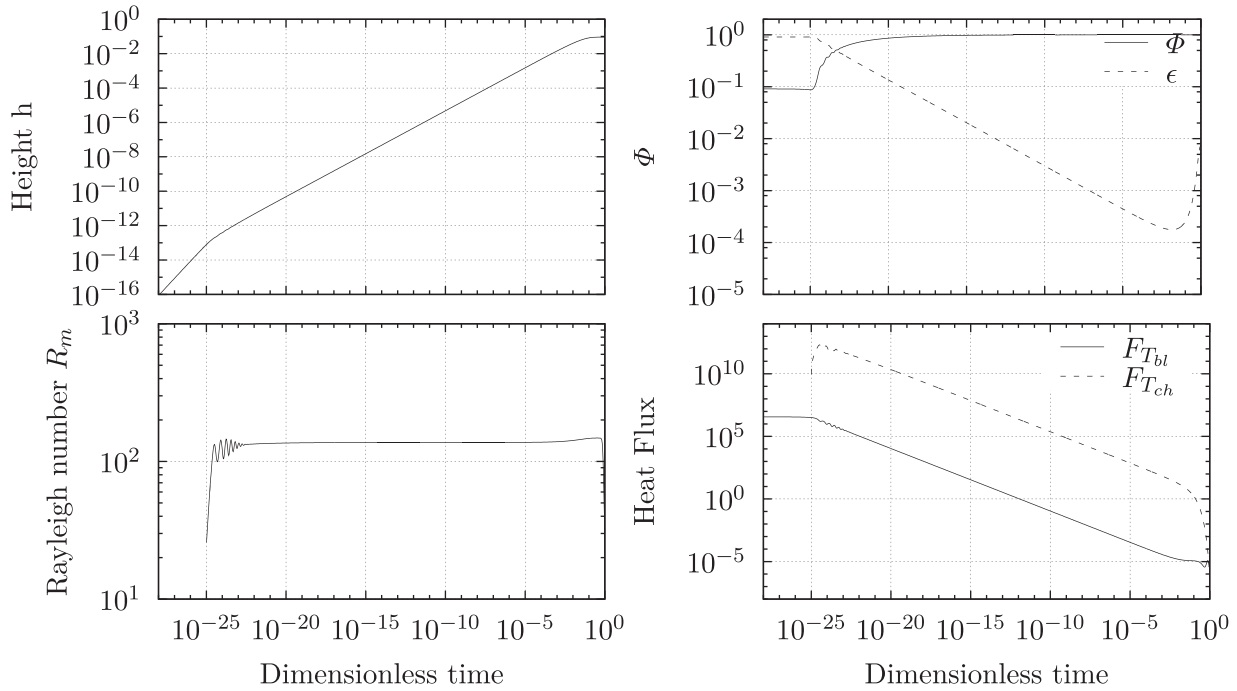


**Figure 22.** Simulation with a set of parameters relevant to the Earth's inner core:  $Nu^* = Nu_\chi = 1.3 \times 10^7$ ,  $\mu = 8.6 \times 10^{11}$ ,  $S = 8.4$  and  $C = 10$ ,  $\gamma = 0.01$ , and  $R = 5.15 \times 10^{16}$ .  $\epsilon$  denotes the porosity ( $\epsilon = (1 - \Phi)$ ).

species conservations, heat and mass transfer at the mush–liquid front and on a relation of kinetic undercooling. A value of the kinetic undercooling parameter has been obtained from our temperature measurements during the initial phase of crystallization. Chimneys observed in the mush at the end of the experiments attest the presence of convection in the mush. However, from our dynamical model and for our experimental parameters, heat and mass transfers at the crystallization front are found to be mostly governed by the boundary-layer mode of convection (between the top of the mush and the liquid bulk). Since the final solid fraction for the maximal apparent gravity level is not very large (about 40 per cent), our model suggests (see analysis of the dynamical model in Section 5) that the final mush height should be proportional to  $g^{-1/3}$  (equivalently, the mass fraction is proportional to  $g^{1/3}$ , which is indeed compatible with our experiments).

The extension of our experiments to the crystallization of the inner core is not straightforward though. Our model (even more so our simplified model in Section 5) is a highly idealized view of the growth of the inner core, however the typical estimates for the relevant dimensionless numbers put them in a regime where convection in the mush must be a dominant feature. Without mush convection (but with the boundary-layer mode), we should expect a small solid fraction of order 0.1. Due to the expected spacing between dendrites, convection in the mush is bound to become very strong and can only be limited by the increase of the solid fraction very near unity. Our numerical model indicates that convection in the mush is likely to produce a solid fraction above 0.95. This value is not due to compaction, and its associated deformation of the solid matrix, which should further increase the solid fraction of the mush.

Except for the averaged solid fraction, our experimental work shows the slow decrease of the interdendritic primary spacing when gravity (and convection effects) is increased. In addition, we have obtained some results on the attenuation of acoustic waves in the mush. Once again, ultrasonic waves (MHz) in a submillimetre microstructure is in rough correspondence with seismic waves (1 s

typical period) in a mush made of 10 m spaced dendrites. Similarly to seismic codas, we detect ultrasonic codas indicating diffusion of sound waves in the mush. We also analyse the attenuation across the mush, between ultrasonic transducers on opposite sides of the mush in a direction perpendicular to the crystallization axis. These results reveal an increase of attenuation (decrease of quality factor) as gravity level and solid fraction increase.

Finally, we have experimental results on the effect of melting the mush from above. They show that the solid fraction in the mush stays constant or increases slightly. However, this is associated with a decrease in attenuation (increase of quality factor). This is surprising as we have observed that attenuation was decreasing with increasing solid fraction (gravity level) in crystallization experiments. Our interpretation is that melting changes the three-dimensional microstructure of the mush in such a way that attenuation is decreased. This is perhaps related to the melting of secondary dendritic arms which can be observed after crystallization experiments and are absent after melting experiments.

The initial motivation for running melting experiments is also related to hemispherical structure of the inner core. The east–west dichotomy on surface velocity and attenuation below the ICB might be related to a model of crystallization/melting (Alboussière *et al.* 2010; Monnereau *et al.* 2010). Attenuation is stronger in the eastern hemisphere compared to the western hemisphere. Based on our attenuation measurement in crystallization and melting experiments, we favour the hypothesis of crystallization on the eastern hemisphere and melting on the western hemisphere. Another argument in favour of the same orientation of the translation mode is based on the fact that stronger buoyancy forces are induced on the melting hemisphere within the translation mode, which can be associated with the stronger anisotropy in the western hemisphere of the inner core (Deguen *et al.* 2013). Finally, recent numerical studies of the dynamics in the outer core have considered an asymmetric buoyant forcing on the ICB (Aubert 2013, 2014; Aubert *et al.* 2013; Davies *et al.* 2013; Deguen *et al.* 2014; Mound *et al.* 2015). They

all reach the conclusion that crystallization on the eastern hemisphere (increased release of buoyant light elements) and melting on the western hemisphere is the preferred scenario to explain features of the outer core flow inferred from geomagnetic studies, such as the large asymmetric gyre (Pais & Jault 2008).

This work is restricted to some aspects only of the general question of the crystallization of the inner core. The geometry is simplified, a simple binary phase diagram is appropriate for ammonium chloride (probably not for the Earth's core), compaction effects are not present in our experiments. Yet, we need at least five dimensionless numbers in an idealized model governing the global evolution of the mush. The complexity of crystallization, with the range of scales between dendritic microstructures, through grains, up to the entire object (the inner core, for instance), precludes full three-dimensional calculations of mush structures and gives an important role to experiments. Adding a new external parameter, gravity, gives more power to experiments as the range of possible crystallization regimes is enlarged.

## ACKNOWLEDGEMENTS

Thanks are due to the Agence Nationale de la Recherche (ANR) (ANR-08-BLAN-0234-01) for financial support. TA acknowledges support from the program PNP of INSU. MB acknowledges support from ENS de Lyon for a visiting fellowship to Lyon. RD gratefully acknowledges support from grant ANR-12-PDOC-0015-01 of the ANR. We thank Marc Moulin, Patrick La Rizza and Jean-Paul Masson for the experimental device development. We thank Ikuro Sumita for the insightful discussions. LH thanks Stéphanie Durand and Benoit Tauzin for the insightful discussions about the seismic attenuation.

## REFERENCES

Aki, K. & Chouet, B., 1975. Origin of coda waves: source, attenuation, and scattering effects, *J. geophys. Res.*, **80**(23), 3322–3342.

Alboussière, T., Deguen, R. & Melzani, M., 2010. Melting-induced stratification above the Earth's inner core due to convective translation, *Nature*, **466**(7307), 744–747.

Alexandrov, D. & Malygin, A., 2011. Coupled convective and morphological instability of the inner core boundary of the Earth, *Phys. Earth planet. Inter.*, **189**(3), 134–141.

Archie, G.E., 1942. The electrical resistivity log as an aid in determining some reservoir characteristics, *Transactions of American Institute of Mining Metallurgical Engineers*, **146**(1), 54–62.

Attanayake, J., Cormier, V.F. & de Silva, S.M., 2014. Uppermost inner core seismic structure—new insights from body waveform inversion, *Earth planet. Sci. Lett.*, **385**, 49–58.

Aubert, J., 2013. Flow throughout the Earth's core inverted from geomagnetic observations and numerical dynamo models, *Geophys. J. Int.*, **192**(2), 537–556.

Aubert, J., 2014. Earth's core internal dynamics 1840–2010 imaged by inverse geodynamo modelling, *Geophys. J. Int.*, **197**(3), 1321–1334.

Aubert, J., Amit, H., Hulot, G. & Olson, P., 2008. Thermo-chemical wind flows couple Earth's inner core growth to mantle heterogeneity, *Nature*, **454**, 758–761.

Aubert, J., Finlay, C.C. & Fournier, A., 2013. Bottom-up control of geomagnetic secular variation by the Earth's inner core, *Nature*, **502**, 219–223.

Baines, W.D. & Turner, J.S., 1969. Turbulent buoyant convection from a source in a confined region, *J. Fluid Mech.*, **37**, 51–80.

Battaille, C.C., Grugel, R., Hmelo, A. & Wang, T., 1994. The effect of enhanced gravity levels on microstructural development in Pb-50 wt pct Sn alloys during controlled directional solidification, *Metall. Mater. Trans. A*, **25**(4), 865–870.

Beckermann, C. & Viskanta, R., 1988. Double-diffusive convection during dendritic solidification of a binary mixture, *PhysicoChemical Hydrodynamics*, **10**(2), 195–213.

Bergman, M.I. & Fearn, D.R., 1994. Chimneys on the Earth's inner-outer core boundary?, *Geophys. Res. Lett.*, **21**(6), 477–480.

Bergman, M.I., Fearn, D.R., Bloxham, J. & Shannon, M.C., 1997. Convection and channel formation in solidifying Pb-Sn alloys, *Metall. Mater. Trans. A*, **28**(3), 859–866.

Bergman, M.I., Macleod-Silberstein, M., Haskel, M., Chandler, B. & Akpan, N., 2005. A laboratory model for solidification of Earth's core, *Phys. Earth planet. Inter.*, **153**(1–3), 150–164.

Blackmore, K., Beatty, K., Hui, M. & Jackson, K., 1997. Growth behavior of  $\text{NH}_4\text{Cl}_2$   $\text{H}_2\text{O}$  mixtures, *J. Cryst. Growth*, **174**(1), 76–81.

Buffett, B.A., Huppert, H.E., Lister, J.R. & Woods, A.W., 1996. On the thermal evolution of the Earth's core, *J. geophys. Res.*, **101**(B4), 7989–8006.

Butler, S.L., 2011. Effective transport rates and transport-induced melting and solidification in mushy layers, *Phys. Fluids*, **23**(1), doi:10.1063/1.3541840.

Butler, S.L., Huppert, H.E. & Worster, M.G., 2006. Numerical modelling of convection in a reactive porous medium with a mobile mush–liquid interface, *J. Fluid Mech.*, **549**, 99–129.

Cao, A. & Romanowicz, B., 2004. Constraints on density and shear velocity contrasts at the inner core boundary, *Geophys. J. Int.*, **157**(3), 1146–1151.

Cao, A., Romanowicz, B. & Takeuchi, N., 2005. An observation of PKJKP: inferences on inner core shear properties, *Science*, **308**(5727), 1453–1455.

Carslaw, H. & Jaeger, J., 1986. *Conduction of Heat in Solids*, 2nd edn, Oxford Science Publications.

Chan, S.-K., Reimer, H.-H. & Kahlweit, M., 1976. On the stationary growth shapes of  $\text{NH}_4\text{Cl}$  dendrites, *J. Cryst. Growth*, **32**(3), 303–315.

Chen, C., 1995. Experimental study of convection in a mushy layer during directional solidification, *J. Fluid Mech.*, **293**, 81–98.

Chen, F., 1997. Formation of double-diffusive layers in the directional solidification of binary solution, *J. Cryst. Growth*, **179**(1–2), 277–286.

Chen, C. & Chen, F., 1991. Experimental study of directional solidification of aqueous ammonium chloride solution, *J. Fluid Mech.*, **227**, 567–586.

Chen, H., Chen, Y.S., Wu, X. & Tewari, S., 2003. History dependence of primary dendrite spacing during directional solidification of binary metallic alloys and interdendritic convection, *J. Cryst. Growth*, **253**(1), 413–423.

Chiarelli, A. & Worster, M.G., 1992. On measurement and prediction of the solid fraction within mushy layers, *J. Cryst. Growth*, **125**(3), 487–494.

Choy, G.L. & Cormier, V.F., 1983. The structure of the inner core inferred from short-period and broadband GDSN data, *Geophys. J. Int.*, **72**(1), 1–21.

Copley, S., Giamei, A.F., Johnson, S. & Hornbecker, M., 1970. The origin of freckles in unidirectionally solidified castings, *Metall. Trans.*, **1**(8), 2193–2204.

Cormier, V.F., 2007. Texture of the uppermost inner core from forward- and back-scattered seismic waves, *Earth planet. Sci. Lett.*, **258**(3), 442–453.

Cummins, P. & Johnson, L.R., 1988a. Synthetic seismograms for an inner core transition of finite thickness, *Geophys. J. Int.*, **94**, 21–34.

Cummins, P. & Johnson, L.R., 1988b. Short-period body wave constraints on properties of the Earth's inner core boundary, *J. geophys. Res.*, **93**(B8), 9058–9074.

Davies, C., Silva, L. & Mound, J., 2013. On the influence of a translating inner core in models of outer core convection, *Phys. Earth planet. Inter.*, **214**, 104–114.

Davis, S.H., 2001. *Theory of Solidification*, Cambridge Univ. Press.

Deguen, R., 2012. Structure and dynamics of Earth's inner core, *Earth planet. Sci. Lett.*, **333**, 211–225.

Deguen, R., Alboussière, T. & Brito, D., 2007. On the existence and structure of a mush at the inner core boundary of the Earth, *Phys. Earth planet. Inter.*, **164**(1), 36–49.

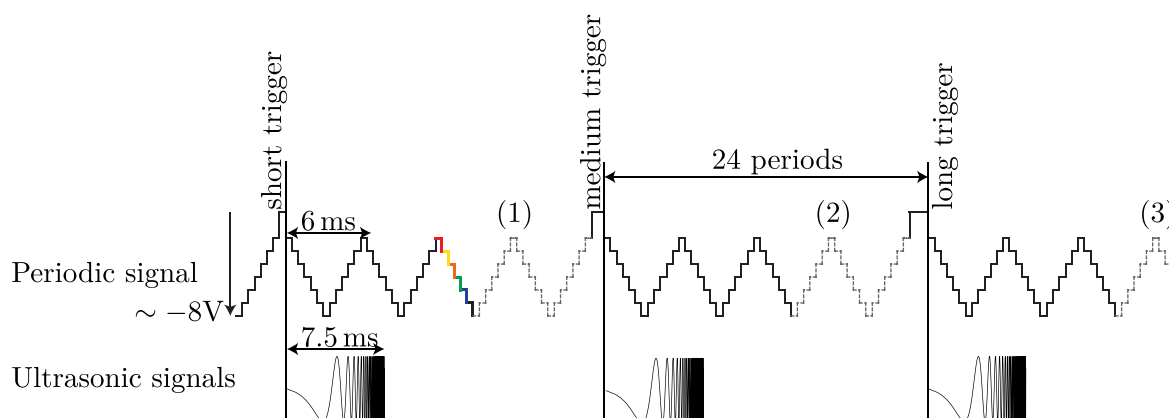
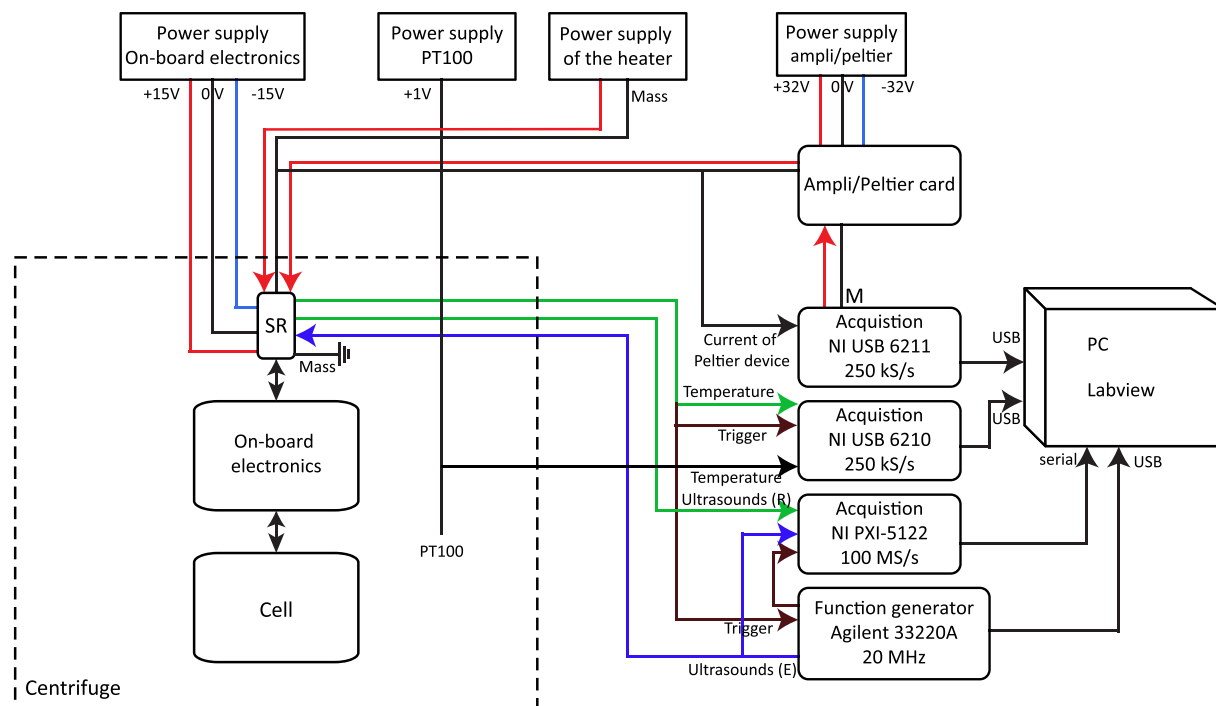
Deguen, R., Alboussière, T. & Cardin, P., 2013. Thermal convection in Earth's inner core with phase change at its boundary, *Geophys. J. Int.*, **194**(3), 1310–1334.

- Deguen, R., Olson, P. & Reynolds, E., 2014. F-layer formation in the outer core with asymmetric inner core growth, *C. R. Geosci.*, **346**(5), 101–109.
- Deuss, A., 2014. Heterogeneity and anisotropy of Earth's inner core, *Annu. Rev. Earth Planet. Sci.*, **42**(1), 103–126.
- Deuss, A., Woodhouse, J.H., Paulssen, H. & Trampert, J., 2000. The observation of inner core shear waves, *Geophys. J. Int.*, **142**(1), 67–73.
- Diepers, H.-J. & Steinbach, I., 2006. Interaction of interdendritic convection and dendritic primary spacing: phase-field simulation and analytical modeling, *Mater. Sci. Forum*, **508**, 145–150.
- Dupouy, M., Camel, D. & Favier, J., 1992. Natural convective effects in directional dendritic solidification of binary metallic alloys: dendritic array primary spacing, *Acta Metall. Mater.*, **40**(7), 1791–1801.
- Dziewonski, A.M. & Anderson, D.L., 1981. Preliminary reference Earth model, *Phys. Earth planet. Inter.*, **25**(4), 297–356.
- Engdahl, E., Flinn, E.A. & Massé, R.P., 1974. Differential PKiKP travel times and the radius of the inner core, *Geophys. J. Int.*, **39**(3), 457–463.
- Engdahl, E.R., Flinn, E.A. & Romney, C.F., 1970. Seismic waves reflected from the Earth's inner core, *Nature*, **228**(5274), 852–853.
- Esbensen, K.H. & Buchwald, V.F., 1982. Planet(oid) core crystallisation and fractionation-evidence from the Agpalilik mass of the Cape York iron meteorite shower, *Phys. Earth planet. Inter.*, **29**(3), 218–232.
- Fearn, D.R., Loper, D.E. & Roberts, P.H., 1981. Structure of the Earth's inner core, *Nature*, **292**, 232–233.
- Gubbins, D., Sreenivasan, B., Mound, J. & Rost, S., 2011. Melting of the Earth's inner core, *Nature*, **473**(7347), 361–363.
- Häge, H., 1983. Velocity constraints for the inner core inferred from long-period PKP amplitudes, *Phys. Earth planet. Inter.*, **31**(2), 171–185.
- Hallworth, M.A., Huppert, H.E. & Woods, A.W., 2004. Crystallization and layering induced by heating a reactive porous medium, *Geophys. Res. Lett.*, **31**(13), doi:10.1029/2004GL019950.
- Hallworth, M.A., Huppert, H.E. & Woods, A.W., 2005. Dissolution-driven convection in a reactive porous medium, *J. Fluid Mech.*, **535**, 255–285.
- Hashin, Z. & Shtrikman, S., 1963. A variational approach to the theory of the elastic behaviour of multiphase materials, *J. Mech. Phys. Solids*, **11**(2), 127–140.
- Huppert, H.E., 1990. The fluid mechanics of solidification, *J. Fluid Mech.*, **212**, 209–240.
- Huppert, H.E. & Turner, J.S., 1981. Double-diffusive convection, *J. Fluid Mech.*, **106**, 299–329.
- Irving, J. & Deuss, A., 2011. Hemispherical structure in inner core velocity anisotropy, *J. geophys. Res.*, **116** (B4), B04307, doi:10.1029/2010JB007942.
- Jackson, K., Hunt, J., Uhlmann, D. & Seward, T., 1966. On origin of equiaxed zone in castings, *Trans. Metall. Soc. AIME*, **236**(2), 139–149.
- Jahrling, K. & Tait, S., 1996. Measurements of the evolution of porosity in a mushy layer, *J. Cryst. Growth*, **167**(1), 285–291.
- Jordan, T.H. & Sipkin, S.A., 1977. Estimation of the attenuation operator for multiple ScS waves, *Geophys. Res. Lett.*, **4**(4), 167–170.
- Kawakatsu, H., 2006. Sharp and seismically transparent inner core boundary region revealed by an entire network observation of near-vertical PKiKP, *Earth Planets Space*, **58**(7), 855–863.
- Kirkpatrick, R.J., Robinson, G.R. & Hays, J.F., 1976. Kinetics of crystal growth from silicate melts: anorthite and diopside, *J. geophys. Res.*, **81**(32), 5715–5720.
- Koper, K.D. & Dombrovskaya, M., 2005. Seismic properties of the inner core boundary from PKiKP/P amplitude ratios, *Earth planet. Sci. Lett.*, **237**(3), 680–694.
- Koper, K.D. & Pyle, M.L., 2004. Observations of PKiKP/PcP amplitude ratios and implications for Earth structure at the boundaries of the liquid core, *J. geophys. Res.*, **109**(B3), doi:10.1029/2003JB002750.
- Koper, K.D., Franks, J.M. & Dombrovskaya, M., 2004. Evidence for small-scale heterogeneity in Earth's inner core from a global study of PKiKP coda waves, *Earth planet. Sci. Lett.*, **228**(3), 227–241.
- Kurz, W. & Fisher, D., 1981. Dendrite growth at the limit of stability: tip radius and spacing, *Acta Metall.*, **29**(1), 11–20.
- Lehmann, P., Moreau, R., Camel, D. & Bolcato, R., 1998. A simple analysis of the effect of convection on the structure of the mushy zone in the case of horizontal Bridgman solidification. Comparison with experimental results, *J. Cryst. Growth*, **183**(4), 690–704.
- Leyton, F. & Koper, K.D., 2007. Using PKiKP coda to determine inner core structure: 2. Determination of QC, *J. geophys. Res.*, **112**(B5), doi:10.1029/2006JB004370.
- Loper, D.E., 1983. Structure of the inner core boundary, *Geophys. Astrophys. Fluid Dyn.*, **25**(1–2), 139–155.
- Loper, D.E. & Fearn, D.R., 1983. A seismic model of a partially molten inner core, *J. geophys. Res.*, **88**(B2), 1235–1242.
- Lum, J.W., 1996. High-speed imaging and analysis of the solidification of undercooled alloy melts, *PhD thesis*, Massachusetts Institute of Technology.
- Lythgoe, K., Deuss, A., Rudge, J. & Neufeld, J., 2013. Earth's inner core: innermost inner core or hemispherical variations?, *Earth planet. Sci. Lett.*, **385**, 181–189.
- Martorell, B., Vočadlo, L., Brodholt, J. & Wood, I.G., 2013. Strong premelting effect in the elastic properties of hcp-Fe under inner-core conditions, *Science*, **342**(6157), 466–468.
- Martorell, B., Brodholt, J., Wood, I.G. & Vočadlo, L., 2015. The elastic properties and stability of fcc-Fe and fcc-FeNi alloys at inner-core conditions, *Geophys. J. Int.*, **202**(1), 94–101.
- Masters, G. & Gubbins, D., 2003. On the resolution of density within the Earth, *Phys. Earth planet. Inter.*, **140**(1), 159–167.
- McDonald, R. & Hunt, J., 1970. Convective fluid motion within the interdendritic liquid of a casting, *Metall. Mater. Trans. B*, **1**(6), 1787–1788.
- Monnereau, M., Calvet, M., Margerin, L. & Souriau, A., 2010. Lopsided growth of Earth's inner core, *Science*, **328**(5981), 1014–1017.
- Morton, B., Taylor, G. & Turner, J., 1956. Turbulent gravitational convection from maintained and instantaneous sources, *Proc. R. Soc. Lond. A*, **234**, 1–23.
- Mound, J., Davies, C. & Silva, L., 2015. Inner core translation and the hemispheric balance of the geomagnetic field, *Earth planet. Sci. Lett.*, **424**(0), 148–157.
- Müller, G. & Neumann, G., 1983. Tenfold growth rates in the travelling heater method of GaSb crystals by forced convection on a centrifuge, *J. Cryst. Growth*, **63**(1), 58–66.
- Mullins, W.W. & Sekerka, R.F., 1964. Stability of a planar interface during solidification of a dilute binary alloy, *J. Appl. Phys.*, **35**, 444–451.
- Okal, E.A. & Cansi, Y., 1998. Detection of PKJKP at intermediate periods by progressive multi-channel correlation, *Earth planet. Sci. Lett.*, **164** (1–2), 23–30.
- O'Rourke, J. *et al.*, 2012. Mushy-layer dynamics in micro and hyper gravity, *Phys. Fluids*, **24**(10), 103305, doi:10.1063/1.4760256.
- Pais, M. & Jault, D., 2008. Quasi-geostrophic flows responsible for the secular variation of the Earth's magnetic field, *Geophys. J. Int.*, **173**(2), 421–443.
- Peppin, S., Huppert, H.E. & Worster, M., 2008. Steady-state solidification of aqueous ammonium chloride, *J. Fluid Mech.*, **599**, 465–476.
- Phinney, R.A., 1970. Reflection of acoustic waves from a continuously varying interfacial region, *Rev. Geophys.*, **8**(3), 517–532.
- Pozzo, M., Davies, C., Gubbins, D. & Alfè, D., 2012. Thermal and electrical conductivity of iron at Earth's core conditions, *Nature*, **485**(7398), 355–358.
- Rees Jones, D.W. & Worster, M.G., 2013. Fluxes through steady chimneys in a mushy layer during binary alloy solidification, *J. Fluid Mech.*, **714**, 127–151.
- Rodot, H., Regel, L. & Turtchaninov, A., 1990. Crystal growth of IV–VI semiconductors in a centrifuge, *J. Cryst. Growth*, **104**(2), 280–284.
- Rodot, H., Regel, L., Sarafanov, G., Hamidi, M., Videskii, I. & Turtchaninov, A., 1986. Cristaux de tellurure de plomb élaborés en centrifugeuse, *J. Cryst. Growth*, **79**(1), 77–83.
- Romanowicz, B. & Mitchell, B., 2007. Q in the Earth from crust to core, *Treatise of Geophysics*, **1**, 731–774.
- Sarazin, J. & Hellawell, A., 1988. Channel formation in Pb–Sb, Pb–Sn, and Pb–Sn–Sb alloy ingots and comparison with the system  $\text{NH}_4\text{Cl–H}_2\text{O}$ , *Metall. Trans. A*, **19**(7), 1861–1871.
- Shearer, P. & Masters, G., 1990. The density and shear velocity contrast at the inner core boundary, *Geophys. J. Int.*, **102**(2), 491–498.

- Shimizu, H., Poirier, J. & Le Mouél, J., 2005. On crystallization at the inner core boundary, *Phys. Earth planet. Inter.*, **151**(1), 37–51.
- Shirtcliffe, T. & Kerr, R.C., 1992. On the use of electrical resistance and temperature as measures of the solid fraction in a mushy layer, *J. Cryst. Growth*, **125**(3), 495–501.
- Shirtcliffe, T., Huppert, H.E. & Worster, M.G., 1991. Measurement of the solid fraction in the crystallization of a binary melt, *J. Cryst. Growth*, **113**(3), 566–574.
- Sipkin, S.A. & Jordan, T.H., 1980. Regional variation of  $Q_{ScS}$ , *Bull. seism. Soc. Am.*, **70**(4), 1071–1102.
- Song, X. & Helmberger, D.V., 1995. Depth dependence of anisotropy of Earth's inner core, *J. geophys. Res.*, **100**(B6), 9805–9816.
- Souriau, A. & Souriau, M., 1989. Ellipticity and density at the inner core boundary from subcritical PKiKP and PcP data, *Geophys. J. Int.*, **98**(1), 39–54.
- Souriau, A. & Poupinet, G., 1991. The velocity profile at the base of the liquid core from PKP(BC+Cdiff) data: an argument in favour of radial inhomogeneity, *Geophys. Res. Lett.*, **18**(11), 2023–2026.
- Spinelli, J., Peres, M. & Garcia, A., 2005. Thermosolutal convective effects on dendritic array spacings in downward transient directional solidification of Al–Si alloys, *J. Alloys Compd.*, **403**(1), 228–238.
- Spinelli, J.E., Rocha, O.F.L. & Garcia, A., 2006. The influence of melt convection on dendritic spacing of downward unsteady-state directionally solidified Sn–Pb alloys, *Mater. Res.*, **9**(1), 51–57.
- Steinbach, I., 2009. Pattern formation in constrained dendritic growth with solutal buoyancy, *Acta Mater.*, **57**(9), 2640–2645.
- Sumita, I. & Olson, P., 1999. A laboratory model for convection in Earth's core driven by a thermally heterogeneous mantle, *Science*, **286**(5444), 1547–1549.
- Sumita, I., Yoshida, S., Kumazawa, M. & Hamano, Y., 1996. A model for sedimentary compaction of a viscous medium and its application to inner-core growth, *Geophys. J. Int.*, **124**(2), 502–524.
- Tait, S. & Jaupart, C., 1989. Compositional convection in viscous melts, *Nature*, **338**, 571–574.
- Tait, S. & Jaupart, C., 1992. Compositional convection in a reactive crystalline mush and melt differentiation, *J. geophys. Res.*, **97**(B5), 6735–6756.
- Tanaka, S. & Hamaguchi, H., 1997. Degree one heterogeneity and hemispherical variation of anisotropy in the inner core from PKP (BC)–PKP DF times, *J. geophys. Res.*, **102**(B2), 2925–2938.
- Tewari, S.N. & Tiwari, R., 2003. A mushy-zone Rayleigh Number to describe interdendritic convection during directional solidification of hypoeutectic Pb–Sb and Pb–Sn alloys, *Metall. Mater. Trans. A*, **34**(10), 2365–2376.
- Tkalčić, H., 2015. Complex inner core of the Earth: the last frontier of global seismology, *Rev. Geophys.*, **53**(1), 59–94.
- Tkalčić, H., Kennett, B.L. & Cormier, V.F., 2009. On the inner–outer core density contrast from PKiKP/PcP amplitude ratios and uncertainties caused by seismic noise, *Geophys. J. Int.*, **179**(1), 425–443.
- Turner, J., 1967. Salt fingers across a density interface, *Deep Sea Research and Oceanographic Abstracts*, **14**(5), 599–611.
- Turner, J.S., 1979. *Buoyancy Effects in Fluids*, Cambridge Univ. Press.
- Viardin, A., Sturz, L., Apel, M. & Hecht, U., 2014. Phase Field Modeling of  $\beta$  (Ti) Solidification in Ti–45at.% Al: columnar dendrite growth at various gravity levels, *Mater. Sci. Forum*, **790**, 34–39.
- Vidale, J.E. & Earle, P.S., 2000. Fine-scale heterogeneity in the Earth's inner core, *Nature*, **404**(6775), 273–275.
- Vočadlo, L., 2007. Ab initio calculations of the elasticity of iron and iron alloys at inner core conditions: evidence for a partially molten inner core?, *Earth planet. Sci. Lett.*, **254**(1–2), 227–232.
- Waszek, L. & Deuss, A., 2011. Distinct layering in the hemispherical seismic velocity structure of Earth's upper inner core, *J. geophys. Res.*, **116**(B12), doi:10.1029/2011JB008650.
- Wells, A., Wettlaufer, J. & Orszag, S., 2010. Maximal potential energy transport: a variational principle for solidification problems, *Phys. Rev. Lett.*, **105**(25), 254502, doi:10.1103/PhysRevLett.105.254502.
- Wells, A., Wettlaufer, J. & Orszag, S., 2011. Brine fluxes from growing sea ice, *Geophys. Res. Lett.*, **38**(4), doi:10.1029/2010GL046288.
- Wells, A.J., Wettlaufer, J.S. & Orszag, S.A., 2013. Nonlinear mushy-layer convection with chimneys: stability and optimal solute fluxes, *J. Fluid Mech.*, **716**, 203–227.
- Whiteoak, S., Huppert, H.E. & Worster, M.G., 2008. Conditions for defect-free solidification of aqueous ammonium chloride in a quasi two-dimensional directional solidification facility, *J. Cryst. Growth*, **310**(15), 3545–3551.
- Woods, A.W. & Huppert, H.E., 1989. The growth of compositionally stratified solid above a horizontal boundary, *J. Fluid Mech.*, **199**, 29–53.
- Worster, M. & Wettlaufer, J., 1997. Natural convection, solute trapping, and channel formation during solidification of saltwater, *J. Phys. Chem. B*, **101**(32), 6132–6136.
- Worster, M.G., 1991. Natural convection in a mushy layer, *J. Fluid Mech.*, **224**, 335–359.
- Worster, M.G., 1992. Instabilities of the liquid and mushy regions during solidification of alloys, *J. Fluid Mech.*, **237**, 649–669.
- Worster, M.G., 1997. Convection in mushy layers, *Annu. Rev. Fluid Mech.*, **29**(1), 91–122.
- Worster, M.G. & Kerr, R.C., 1994. The transient behaviour of alloys solidified from below prior to the formation of chimneys, *J. Fluid Mech.*, **269**, 23–44.
- Worster, M.G., Huppert, H.E. & Sparks, R.S.J., 1990. Convection and crystallization in magma cooled from above, *Earth planet. Sci. Lett.*, **101**(1), 78–89.
- Worster, M.G., Huppert, H.E. & Sparks, R.S.J., 1993. The crystallization of lava lakes, *J. geophys. Res.*, **98**(B9), 15 891–15 901.
- Yu, J., Bergman, M.I., Huguet, L. & Alboussiere, T., 2015. Partial melting of a Pb–Sn mushy layer due to heating from above, and implications for regional melting of Earth's directionally solidified inner core, *Geophys. Res. Lett.*, **42**, 7046–7053.
- Yu, W.-C., Wen, L. & Niu, F., 2005. Seismic velocity structure in the Earth's outer core, *J. geophys. Res.*, **110**(B2), doi:10.1029/2003JB002928.
- Zeng, X. & Ni, S., 2013. Constraining shear wave velocity and density contrast at the inner core boundary with PKiKP/P amplitude ratio, *J. Earth Sci.*, **24**(5), 716–724.

## APPENDIX A: EXPERIMENTAL ACQUISITION PROTOCOL

Here, we describe our experimental acquisition protocol. To collect the data during rotation, we have used small and high-speed slip rings (MOOG EC3848) which is limited to 10 wires. This bound implies to use an on-board electronic which allows the multiplexing of all signals. Fig. A1 shows a sketch of data acquisition. Four power generators supply the on-board electronics, the heater, the amplifier and one temperature probe respectively. The ultrasound signal is generated by the waveform function generator (Agilent 33220A) and is amplified by the on-board electronics. The ultrasonic signals, the temperature signal and the current of the Peltier device are recorded by the acquisition cards (NI-6211, NI-6210, NI PXI-5122). To maintain a constant temperature at the bottom of the cell, we have used a Peltier element with a PID controller, that is, a control loop feedback mechanism. The Peltier voltage is delivered by the NI-6211 card through the voltage amplifiers (Ampli/Peltier card in Fig. A1). On the on-board electronic card, voltage amplifiers are used for the ultrasonic signals before emission and after reception to increase the ratio signal/noise. A microcontroller allows the multiplexing of the temperature signals. It generates a step periodical signal which contains the temperature signals and the trigger (Fig. A2), which is composed of 24 6 ms-periods between each trigger. Each step of the half-period corresponds to the voltage measured across one of the PT100 probe (colours corresponds to temperature probes in Fig. 3). The mean of each step during  $24 \times 6$  ms gives us the voltage across each temperature probes and the temperature.



Moreover, there are three different trigger signals—short ((1) in Fig. A2), medium ((2) in Fig. A2) and long ((3) in Fig. A2) that correspond to the emission/reception of the ultrasonic signal at one of the three different pairs (Fig. A2). Moreover, there are three differ-